Posted on 4 May 2023 — The copyright holder is the author/funder. All rights reserved. No reuse without permission. — https://doi.org/10.22541/essoar.168319846.64187871/v1 — This a preprint and has not been peer reviewed. Data may be preliminary.

Enhancing regional seismic velocity model with higher-resolution local results using sparse dictionary learning

Hao Zhang[1] and Yehuda Ben-Zion[1]

[1]University of Southern California

May 4, 2023

Abstract

We use sparse dictionary learning to develop transformations between seismic velocity models of different resolution and spatial extent. Starting with results in the common region of both models, the method can be used to enhance a regional lower-resolution model to match the style and resolution of local higher-resolution results while preserving its regional coverage. The method is demonstrated by applying it to two-dimensional Vs and three-dimensional VP and VS local and regional velocity models in southern California. The enhanced reconstructed models exhibit clear visual improvements, especially in the reconstructed VP/VS ratios, and better correlations with geological features. We demonstrate the improvements of the reconstructed model relative to the original velocity model by comparing waveform simulation results to observations. The improved fitting to observed waveforms extends beyond the domain of the overlapping region. The developed dictionary learning approach provides physically interpretable results and offers a powerful tool for additional applications for data enhancement in earth sciences.

Enhancing regional seismic velocity model with higher-resolution local results using sparse dictionary learning

Hao Zhang[1] **and Yehuda Ben-Zion**[1,2]

[1]Department of Earth Sciences, University of Southern California, Los Angeles, California, USA
[2]Southern California Earthquake Center, University of Southern California, Los Angeles, California, USA

Key Points:

- We present a new method for merging multi-scale velocity models with different resolutions.
- We reconstruct a high resolution regional seismic velocity model for southern California.
- Validation with waveform simulations shows that the reconstructed model outperforms the original model.

Corresponding author: Hao Zhang, hzhang63@usc.edu

Abstract

We use sparse dictionary learning to develop transformations between seismic velocity models of different resolution and spatial extent. Starting with results in the common region of both models, the method can be used to enhance a regional lower-resolution model to match the style and resolution of local higher-resolution results while preserving its regional coverage. The method is demonstrated by applying it to two-dimensional V_s and three-dimensional V_P and V_S local and regional velocity models in southern California. The enhanced reconstructed models exhibit clear visual improvements, especially in the reconstructed V_P/V_S ratios, and better correlations with geological features. We demonstrate the improvements of the reconstructed model relative to the original velocity model by comparing waveform simulation results to observations. The improved fitting to observed waveforms extends beyond the domain of the overlapping region. The developed dictionary learning approach provides physically interpretable results and offers a powerful tool for additional applications for data enhancement in earth sciences.

Plain Language Summary

Seismic velocity models are essential for many applications including derivation of earthquake properties, studies of tectonic processes, and analysis of earthquake ground motions. In various places there are velocity models of different spatial coverage and resolution. To benefit from the complementary strengths of such models, we develop a new method for enhancing regional velocity models of relatively low-resolution with information contained in local higher-resolution models. The method builds a transformation between different models in their common local region based on a sparse dictionary learning and then uses the transformation outside the common region. We apply the method to seismic velocity models in southern California and show that the enhanced regional model outperforms the original velocity model in fitting earthquake waveforms and also has better consistency with geological features. The method has a potential for improving the quality of other data sets in earth science.

1 Introduction

Seismic velocity models are foundational to numerous applications including derivations of earthquake source properties, simulations of seismic ground motion from scenario earthquakes, and a broad range of structural and tectonophysics topics. The spatial coverage and resolution of derived velocity models depend on the data and inversion methods used, and models of widely different scales and resolutions are often available in well-studied regions. In southern California, there are several regional velocity models with a nominal resolution of about 5 km (e.g. Lee et al., 2014; Shaw et al., 2015; Fang et al., 2022), along with models focusing on the San Jacinto and San Andreas faults with a nominal resolution of 2-3 km (e.g. Allam & Ben-Zion, 2012; Zigone et al., 2015; Fang et al., 2019; Share et al., 2019). More local models based on dense array data can have resolution approaching tens of meters (e.g. Hillers et al., 2016; Mordret et al., 2019) and results based on borehole data can resolve sub-cm features (e.g. Gibbs et al., 2001; Bonilla et al., 2002). Developing methods to merge velocity models of different scales and resolutions can provide multi-scale frameworks that benefit from the complementary strengths of the different results.

The most straightforward approach to combine models is to embed small-scale high-resolution velocity models within regional models and smooth the boundaries (e.g. Fichtner et al., 2018; Ajala & Persaud, 2021). While this approach is simple, the obtained seismic velocities near the boundaries between models depend on ad-hoc choices of the applied smoothing parameters. Importantly, local perturbations to seismic wavefields generated near the boundaries between models can affect the seismic wavefield on a regional scale (e.g. Juarez & Ben-Zion, 2020; Ajala & Persaud, 2021; Yeh & Olsen, 2022). Furthermore, embedding only updates the low-resolution model in the area covered by the high-resolution results, without enhancing the outer region, and such procedures disregard useful information from the low-resolution results in the area covered by the high-resolution model. In the present study we develop a method for merging multi-scale velocity models by establishing a transformation between models of different resolutions. Specifically, we develop a transformation by comparing high- and low- resolution imaging results in a given region and then utilize this transformation to enhance the low-resolution model both in the overlapping region as well as outside it.

The developed methodology is inspired by progress made in machine learning algorithms for super-resolution (Dong et al., 2015) and style transfer (Gatys et al., 2016) of images. To merge seismic velocity models, we use a data-driven approach based on sparse dictionary learning (Yang et al., 2008; Mairal et al., 2009). Since the available amount of data is limited, we opt for this approach over Convolutional Neural Networks (CNN) that demand a large number of trainable parameters. Dictionary learning involves a linear decomposition of an input signal utilizing a small set of basis signals, referred to as atoms, which are learned from the data. This technique has achieved impressive outcomes in various image and video processing tasks. In seismology, dictionary learning was used for signal denoising (Beckouche & Ma, 2014) and for seismic tomography (Bianco & Gerstoft, 2018). Dictionary learning has the added benefits of being physically interpretable (in contrast to CNN), and better generalization capability than CNN when the dataset is limited (Sulam et al., 2020).

In the following sections, we first introduce a framework for representing seismic velocity models using dictionaries and subsequently devise a method for developing a transformation between models that can enrich the lower-resolution model. As initial applications, we implement the technique on both 2D and 3D velocity models in southern California with different resolution and spatial extent. We generate an enhanced reconstructed version of the regional community velocity model CVM-S4.26 (Lee et al., 2014) utilizing a higher-resolution model around the San Jacinto fault zone (Fang et al., 2019), and demonstrate by comparing waveform simulations with observations that the reconstructed model outperforms the original version.

2 Methods

2.1 Dictionary representation of velocity models

Dictionary Learning involves identifying a sparse representation of input data in the form of a linear combination of basis atoms inferred from the input data (Mairal et al., 2009), and it provided important results in compressed sensing and signal recovery. In this section, we present a novel method for applications on merging and enhancing seismic velocity models.

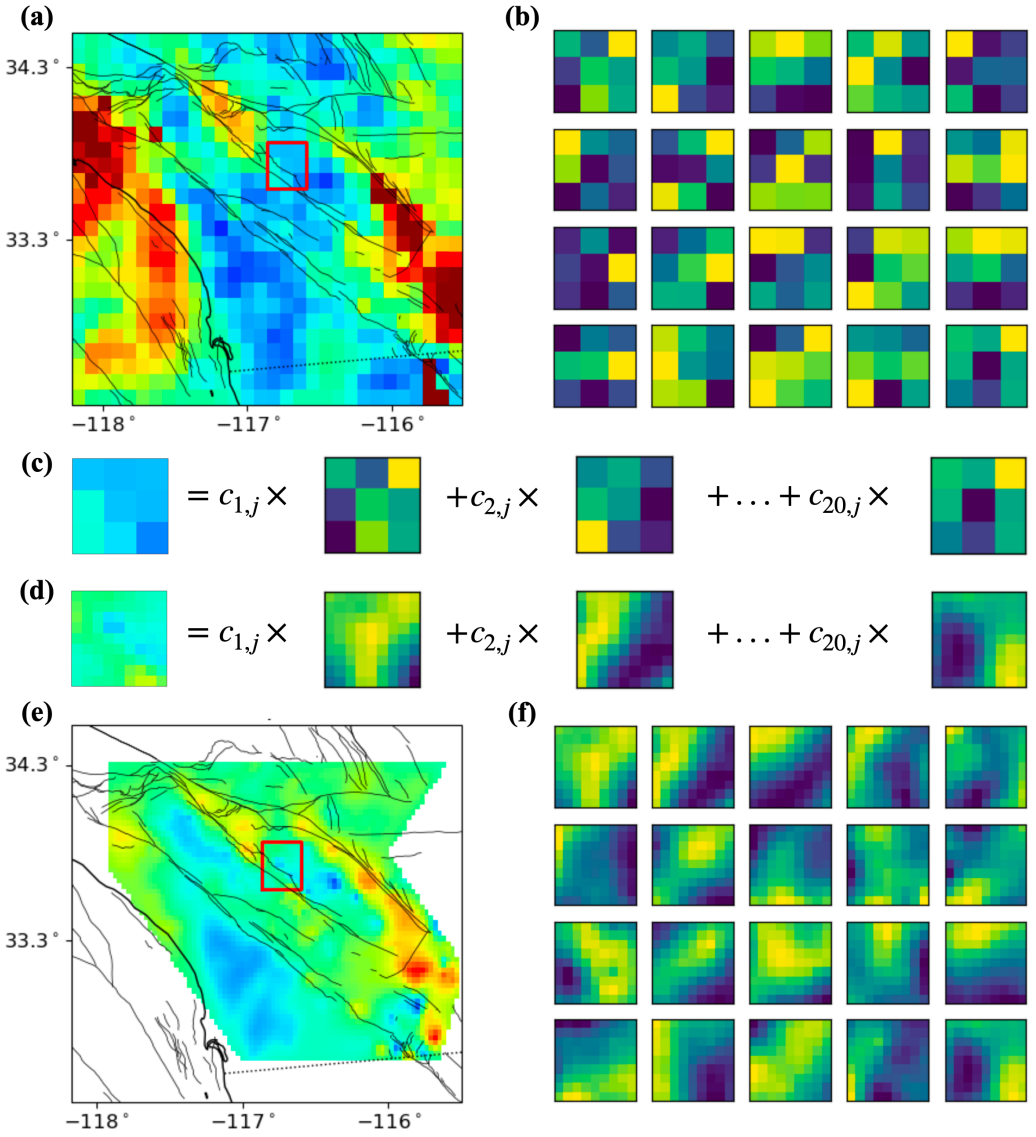

Figure 1. Dictionary representation of seismic velocity models and transformation between them. **(a)** Horizontal slice of CVM-S4.26 at 2 km depth with a resolution of $0.09° \times 0.09°$. The red square indicates the patch used in (c). **(b)** A dictionary consisting of 20 atoms learned from the velocity model in (a). **(c)** Each patch extracted from the velocity model can be represented as a linear superposition of atoms in the dictionary. **(d)** The patch extracted from the model in (e) at the same location can be represented using another dictionary with the same sparse representation. **(e)** Horizontal slice of the Fang et al. (2019) model in the same region as (a) but with higher-resolution. **(f)** A dictionary learned from the velocity model in (e). All atoms are reshaped to the window size for better visualization.

Seismic velocity models are represented as 2D or 3D grids that contain information about P wave velocity V_P and/or S wave velocity V_S at a set of specific spatial locations. Given a seismic velocity model $\mathcal{M}$, we can utilize a sliding window which has the same dimension as the model to extract patches from it, resulting in N patches $\boldsymbol{p}_1, ..., \boldsymbol{p}_N$ that represent values inside subsections of the model (Figure 1a). To simplify the description, we flatten each patch into a 1D array with length L representing the number of grids within the window (Dong et al., 2015). For example, $L = 9$ if the size of a 2D window is 3×3, and $L = 90$ if the window is a $3 \times 3 \times 10$ cube. The set of flattened patches is denoted as $\mathbf{P} \in \mathbb{R}^{L \times N}$.

The dictionary representation of the seismic velocity model is used to find a linear relationship among the patches in $\mathbf{P}$ and their low-dimensional projections, i.e., a dictionary $\mathbf{D}^* = [\boldsymbol{d}_1, ..., \boldsymbol{d}_K] \in \mathbb{R}^{L \times K}$ contains K prototype atoms (with $K < N$ usually), each with the same length as the patches (Figure 1b). Each patch $\boldsymbol{p}_j \in \mathbb{R}^L$ can be represented as a sparse linear combination of the atoms in $\mathbf{D}^*$:

$$\boldsymbol{p}_j \approx \mathbf{D}^* \boldsymbol{c}_j = \sum_{i=1}^{K} c_{i,j} \boldsymbol{d}_i, \tag{1}$$

where $\boldsymbol{c}_j = [c_{1,j}, ..., c_{K,j}]^T$ and $c_{i,j}$ and $c_{i,j}$ represents the sparse coefficients for patches $\boldsymbol{p}_j$ for atoms $\boldsymbol{d}_i$ (Figure 1c). These linear combinations can be written in a matrix form as

$$\mathbf{P} \approx \mathbf{D}^* \mathbf{C}^*, \tag{2}$$

where $\mathbf{C}^* = [\boldsymbol{c}_1, ..., \boldsymbol{c}_N] \in \mathbb{R}^{K \times N}$ is the sparse representation matrix with very few nonzero entries (Kreutz-Delgado et al., 2003).

To solve the dictionary $\mathbf{D}^*$ and coefficients $\mathbf{C}^*$ from patches, we use a sparse coding algorithm (e.g. Rubinstein et al., 2010) that seeks to minimize the difference between the patches and the reconstruction from linear superposition

$$\mathbf{D}^*, \mathbf{C}^* = \underset{\mathbf{D},\mathbf{C}}{\operatorname{argmin}} \|\mathbf{P} - \mathbf{D}\mathbf{C}\|_2^2 + \lambda \|\mathbf{C}\|_0. \tag{3}$$

where $\|\cdot\|_2$ and $\|\cdot\|_0$ are the second and zero order norm, respectively. The regularization parameter λ controls the tradeoff between the sparsity and the minimization error. Various algorithms, such as Orthogonal Matching Pursuit (OMP) (Mallat & Zhang, 1993) and Least Absolute Shrinkage and Selection Operator (LASSO) Tibshirani (1996), can be used to solve this optimization problem (3). After obtaining the dictionary $\mathbf{D}^*$ and corresponding representation matrix $\mathbf{C}^*$ using the sparse coding algorithm, the reconstructed patches is calculated as $\hat{\mathbf{P}} = \mathbf{D}^*\mathbf{C}^*$. The updated velocity model can be then developed by stitching the reconstructed patches together in their original spatial order (Dong et al., 2015).

2.2 Transformation between two seismic velocity models

The dictionary representation technique can facilitate the transformation between two different seismic velocity models by establishing a correspondence between their respective dictionaries. Suppose we have an initial model $\mathcal{M}_1$ and a second more local model $\mathcal{M}_2$ with a higher-resolution that is spatially included in $\mathcal{M}_1$ (Figure 1a,e). Our goal is to transform $\mathcal{M}_1$ to model $\hat{\mathcal{M}}$, with resolution and values in the common region of both models consistent with $\mathcal{M}_2$ and enhanced resolution outside the overlapping region. Essentially, this transformation should improve $\mathcal{M}_1$ to match the resolution and style of $\mathcal{M}_2$ while preserving its coverage.

To solve the problem described above, we divide it into three steps. In the first step, we extract patches $\mathbf{P}_1^{\mathrm{U}} = [\boldsymbol{p}_1^1, ..., \boldsymbol{p}_1^{N_1}] \in \mathbb{R}^{L_1 \times N_1}$ from the entire $\mathcal{M}_1$. A subset of $\mathbf{P}_1^{\mathrm{U}}$, $\mathbf{P}_1 = [\boldsymbol{p}_1^1, ..., \boldsymbol{p}_1^{N_2}] \in \mathbb{R}^{L_1 \times N_2}$ shares spatial locations with patches $\mathbf{P}_2 = [\boldsymbol{p}_2^1, ..., \boldsymbol{p}_2^{N_2}] \in \mathbb{R}^{L_1 \times N_2}$ extracted from $\mathcal{M}_2$. Such pairs of patches, e.g., $\boldsymbol{p}_1^i$ and $\boldsymbol{p}_2^i$, extracted from the same spatial locations are aligned by their index in $\mathbf{P}_1$ and $\mathbf{P}_2$. The length of the patches, L_1 and L_2, may differ due to the different resolution of $\mathcal{M}_1$ and $\mathcal{M}_2$. In the second step, we transfer the patches from $\mathbf{P}_1^{\mathrm{U}}$ to $\hat{\mathbf{P}}$ to ensure that under this transformation the transformed $\mathbf{P}_1$ is consistent with $\mathbf{P}_2$. Finally, the transformed patches $\hat{\mathbf{P}}$ are put back to their original spatial location to rebuild the transformed velocity model $\hat{\mathcal{M}}$.

The dictionary representation technique described in section 2.1 is applied in the second step, i.e., the transformation of patches from $\mathbf{P}_1^{\mathrm{U}}$ to $\hat{\mathbf{P}}$. First, we represent patches in $\mathbf{P}_1$ as sparse linear combination of K atoms in a dictionary $\mathbf{D}_1 = [\boldsymbol{d}_1^1, ..., \boldsymbol{d}_1^K] \in \mathbb{R}^{L_1 \times K}$

$$\mathbf{P}_1 \approx \mathbf{D}_1 \mathbf{C}. \tag{4}$$

This produces a sparse representation $\mathbf{C} \in \mathbb{R}^{K \times N_2}$ that contains the sparse coefficients for each patch in $\mathbf{P}_1$ (Figure 1c). The dictionary $\mathbf{D}_1$ and the sparse representation $\mathbf{C}$ can be obtained simultaneously using sparse coding algorithms (section 2.1). We also represent the patches in $\mathbf{P}_2$ as a linear combination of atoms in a second (higher-resolution) dictionary $\mathbf{D}_2 = [\boldsymbol{d}_2^1, ..., \boldsymbol{d}_2^K] \in \mathbb{R}^{L_2 \times K}$ with the same sparse representation $\mathbf{C}$ (Figure 1d,f)

$$\mathbf{P}_2 \approx \mathbf{D}_2 \mathbf{C}. \tag{5}$$

The atom $\boldsymbol{d}_2^j$ in $\mathbf{D}_2$ have one-to-one corresponding to $\boldsymbol{d}_1^j$ in $\mathbf{D}_1$ due to the duality between $\mathbf{P}_1$ and $\mathbf{P}_2$. Therefore, we can first represent $\mathbf{P}_1^{\mathrm{U}}$ on $\mathbf{D}_1$ using a representation matrix $\mathbf{C}^{\mathrm{U}}$ and then construct the transferred patches $\hat{\mathbf{P}} = \mathbf{D}_2 \mathbf{C}^{\mathrm{U}}$.

In practice, we randomly divide the patches $\mathbf{P}_1$ and $\mathbf{P}_2$ into training set $\mathbf{P}_1^{\mathrm{T}}$, $\mathbf{P}_2^{\mathrm{T}}$ and validation set $\mathbf{P}_1^{\mathrm{V}}$, $\mathbf{P}_2^{\mathrm{V}}$, and put each pair of patches with the same location in the same dataset. The training set is utilized to learn the dictionary and sparse representation matrix, while the validation set is used to select optimal parameters. We use the OMP algorithm to obtain the dictionary $\mathbf{D}_1$ for the train set $\mathbf{P}_1^{\mathrm{T}}$ and the corresponding sparse representation $\mathbf{C}^{\mathrm{T}}$ from following optimization:

$$\mathbf{D}_1, \mathbf{C}^{\mathrm{T}} = \underset{\mathbf{D},\mathbf{C}}{\operatorname{argmin}} \|\mathbf{P}_1^{\mathrm{T}} - \mathbf{D}\mathbf{C}\|_2^2 + \lambda \|\mathbf{C}\|_0. \tag{6}$$

For the derived sparse representation $\mathbf{C}^{\mathrm{T}}$, we calculate the corresponding dictionary

$$\mathbf{D}_2 = \underset{\mathbf{D}}{\operatorname{argmin}} \|\mathbf{P}_2^{\mathrm{T}} - \mathbf{D}\mathbf{C}^{\mathrm{T}}\|_2^2 \tag{7}$$

from $\mathbf{P}_2^{\mathrm{T}}$ using the Least Squares Method. Then we use the validation set to evaluate the performance of the trained dictionaries $\mathbf{D}_1$ and $\mathbf{D}_2$. The patches in $\mathbf{P}_1^{\mathrm{V}}$ are represented on the trained $\mathbf{D}_1$ using a sparse representation

$$\mathbf{C}^{\mathrm{V}} = \underset{\mathbf{C}}{\operatorname{argmin}} \|\mathbf{P}_1^{\mathrm{V}} - \mathbf{D}_1\mathbf{C}\|_2^2 + \lambda \|\mathbf{C}\|_0. \tag{8}$$

We then compare the difference between the transferred validation set $\hat{\mathbf{P}}^{\mathrm{V}} = \mathbf{D}_2 \mathbf{C}^{\mathrm{V}}$ and $\mathbf{P}_2^{\mathrm{V}}$. The difference between patches $\mathbf{P}$ and the baseline patches $\mathbf{P}_0$ is defined as

$$D(\mathbf{P}, \mathbf{P}_0) = \frac{\|\mathbf{P} - \mathbf{P}_0\|_2}{\|\mathbf{P}_0\|_2}. \tag{9}$$

The optimal hyper-parameters in the training procedure (e.g, the K number of atoms in a dictionary and the sparsity control parameter λ) are found by minimizing the difference $D(\hat{\mathbf{P}}^{\mathrm{V}}, \mathbf{P}_2^{\mathrm{V}})$.

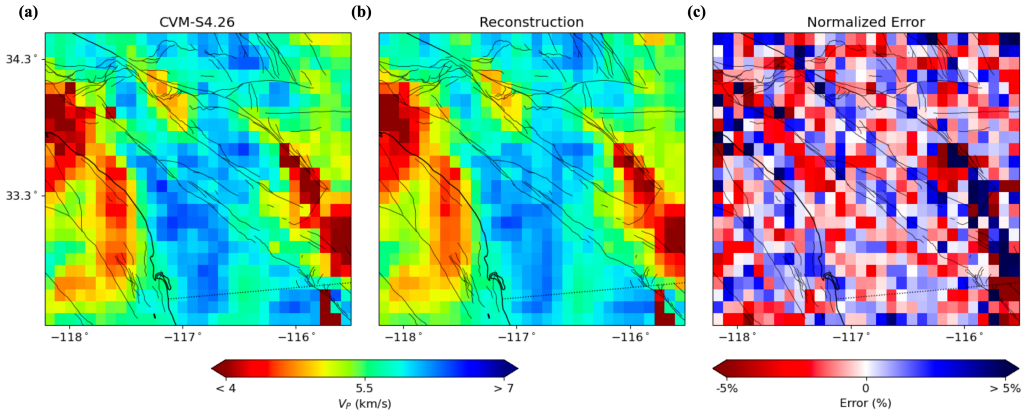

Figure 2. **(a)** Horizontal slice of V_p at 2 km depth from CVM-S4.26. The sampled resolution is $0.09° \times 0.09°$. **(b)** Reconstruction of the model in (a) using a dictionary representation. **(c)** The difference (error) between the reconstruction and the original model normalized at each grid by the value in the original model. Black lines mark major fault traces.

3 Results

3.1 Capability of the dictionary representation

As the basis of our methodology for transforming seismic velocity models, we first demonstrate the capability of representing a seismic velocity model using a dictionary with minimal error. We use a horizontal slice of V_P at 2 km depth from the CVM-S4.26 model (Lee et al., 2014) as an example (Figure 2a). This waveform-based community velocity model for southern California was shown to have a good overall performance in a validation study using waveform simulations (Lu & Ben-Zion, 2022). With a horizontal resolution of $0.09° \times 0.09°$, there are 30 grid points along the longitude direction and 24 grid points along the latitude direction in this horizontal slice.

We extract 616 patches from this model using a sliding window of size 3×3 and a stride (amount of grid points of window's movement over the model in one direction) of 1. In the training of the dictionary using OMP, we set the regularization parameter λ as 0.1 and the number of atoms in the dictionary to be 20 (Figure 1b). The resulting sparse representation of the model in the dictionary is then used to reconstruct the model (Figure 2b). The average error between the reconstruction and the original model is 2.2% while the peak error at a single grid is 7%, demonstrating accurate reconstruction using the dictionary representation. We applied the dictionary representation to other 2D or 3D velocity models utilized in this study and the resulting errors are found to be consistently small.

3.2 Transformation between 2D V_S models

In this section, we evaluate the performance of the method for 2D sections of V_S results. Zigone et al. (2015) derived a 3D V_S model around the San Jacinto and San Andreas faults in Southern California from Rayleigh wave velocities constructed from the ambient seismic noise. The model, referred to below as Z2015 and chosen as the target model $\mathcal{M}_2$, has high-resolution in the top 7 km. As illustrated in Figure 3a with a horizontal slice at a

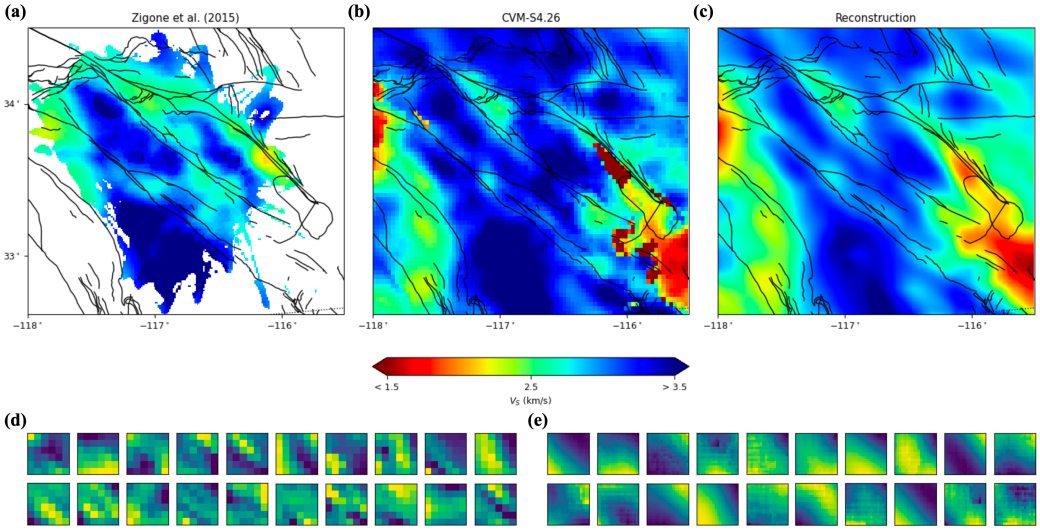

Figure 3. **(a-c)** Horizontal slices of V_S at 2 km depth from the Z2015 model (a), CVM-S4.26 (b), and the reconstructed model (c). The resolution of the Z2015 and reconstructed models is $0.01^\circ \times 0.01^\circ$, while the resolution of CVMS is $0.03^\circ \times 0.03^\circ$. Black lines show major fault traces. **(d)** low-resolution dictionary $\mathbf{D}_1$ and **(e)** high-resolution dictionary $\mathbf{D}_2$ learned from the training data. All atoms are reshaped to the window size for better visualization.

depth of 2 km, the results exhibit informative lateral variations including low velocity zones and velocity contrasts across the main faults. On the other hand, the regional model CVM-S4.26 used as the initial model $\mathcal{M}_1$ shows clearly low velocity sediments in the Salton Trough (Figure 3b), outside the spatial extent of Z2015. The horizontal resolution of $\mathcal{M}_1$ and $\mathcal{M}_2$ are $0.03^\circ \times 0.03^\circ$ and $0.01^\circ \times 0.01^\circ$, respectively, and the range of CVM-S4.26 used in the analysis is larger than that of $\mathcal{M}_2$ (Figures 3a,b).

Patches are extracted from the overlapping area using a 6×6 sliding square window on $\mathcal{M}_1$ with a stride of 1 and a 18×18 sliding window on $\mathcal{M}_2$ with a stride of 3. To have efficient training of dictionaries, we compute the cross-correlation (CC) between upsampled low-resolution patches and their corresponding high-resolution patches. We only utilize patch pairs with $CC > 0$ for both training and validation. Following this selection process, 1131 patch pairs are available for analysis in this example application, from which we randomly select 1000 pairs as the training set $\mathbf{P}_1^{\mathrm{T}}$ and $\mathbf{P}_2^{\mathrm{T}}$, while the remaining pairs are allocated for the validation set $\mathbf{P}_1^{\mathrm{V}}$ and $\mathbf{P}_2^{\mathrm{V}}$.

Out of 40 combinations of hyperparameter configurations, the optimal number of atoms in $\mathbf{D}_1$ and $\mathbf{D}_2$ is determined to be 20, with an optimal sparsity control factor of 0.1. The dictionaries that were trained are presented in Figures 3d,e. Notably, there is a coherence between the texture of atom pairs in the low-resolution dictionary $\mathbf{D}_1$ and the high-resolution dictionary $\mathbf{D}_2$. This coherence is learned from the patches spontaneously rather than predefined. The difference between $\mathbf{P}_2^{\mathrm{T}}$ and the transformed $\hat{\mathbf{P}}_1^{\mathrm{T}}$ is 6.1%, while the difference between $\mathbf{P}_2^{\mathrm{V}}$ and the transformed $\hat{\mathbf{P}}_1^{\mathrm{V}}$ is 7.6%. To evaluate the performance of trained dictionaries, we upsample $\mathcal{M}_1$ to the same resolution as $\mathcal{M}_2$ using bicubic interpolation, and the difference between $\mathcal{M}_2$ and the upsampled $\mathcal{M}_1$ in the overlapping region is 11.55%. The

difference between models decreases on both training and validation sets, indicating the effectiveness of the method. Subsequently, the transformation is applied to the entire region of $\mathcal{M}_1$, and the reconstructed model is shown in Figure 3c. This model is smoother than CVM-S4.26 in the entire domain (Figure 3b) and more consistent with the Z2015 model in the common region. Additionally, the reconstructed model shows a good consistency with geological features, e.g., low velocities around both the San Jacinto and San Andreas faults.

3.3 Transformation between both 3D V_P and V_S models

To demonstrate more general application scenarios, we show the efficacy of our methodology by analyzing 3D velocity models that incorporate both V_P and V_S. Merging and enhancing 3D models can improve derivation of earthquake source properties, simulations of ground motion, and other applications. Additionally, the V_P/V_S ratio is an important parameter that provides key information on various geological and mechanical aspects such as lithology, rock damage, partial melting and water saturation. A seismic velocity model of high quality should display coherent geological features in the V_P/V_S ratios.

Fang et al. (2019) developed a joint inversion technique that utilizes both body and surface wave data to improve the resolution of V_P (Figure 4, middle row) and VS (Figure 5, middle row). The resulting velocity model (referred to as F2019) exhibits distinct regions of V_P/V_S ratios along the coast, in the vicinity of the San Jacinto and San Andreas faults, and the Salton Sea regions (Figure 6, middle row). In contrast, the regional seismic tomography model CVM-S4.26 lacks coherent regions of V_P/V_S ratios consistent with geological features (Figure 6, top row). When transforming an under-constrained V_P/V_S ratio model to a well-constrained model, it is important to verify that the resulting V_P/V_S ratios correlate well with geological features.

In this case study, the initial seismic velocity model $\mathcal{M}_1$ is taken from velocities at 5 different depth sections (1, 2, 3, 4, and 5 km) of the CVM-S4.26, while the target model $\mathcal{M}_2$ is taken from velocities of the F2019 model at the same depths. Both models have two sets of velocities, V_P and V_S, with a total of 10 layers representing values at different depths. The horizontal resolution resolutions of $\mathcal{M}_1$ and $\mathcal{M}_2$ are $0.09^\circ \times 0.09^\circ$ and $0.03^\circ \times 0.03^\circ$, respectively. To ensure the smoothness of the transformed model, we employ bicubic interpolation to upsample $\mathcal{M}_1$ to match the horizontal resolution of $\mathcal{M}_2$. We then extract patches from both models using a $9 \times 9 \times 10$ sliding window (10 being the number of layers) with a stride of 1. The resulting patch pairs total 980, from which 800 are randomly selected for the training set and the remaining pairs are used for validation. Each of our trained dictionaries contain 20 atoms with a dimension of $9 \times 9 \times 10$. After transformation, the difference between $\mathbf{P}_2^{\mathrm{T}}$ and the transformed $\hat{\mathbf{P}}_1^{\mathrm{T}}$ is 2.9%, while the difference between $\mathbf{P}_2^{\mathrm{V}}$ and the transformed $\hat{\mathbf{P}}_1^{\mathrm{V}}$ is 3.4%. As a baseline, the difference between patches extracted from $\mathcal{M}_1$ and $\mathcal{M}_2$ in the overlapping region is 8.1%. Both reconstructions of training and validation patches are more consistent with the target model, compared to the initial model.

The reconstructed V_P/V_S exhibits significant visual improvements with respect to the initial model and enhanced similarity to the target model. The updated regional V_P/V_S results display clearly several zones with coherent values (Figure 6, bottom row), which extend the correlations with geological characteristics shown in the F2019 model. The coherence is also clear in a cross-section that traverses both the San Jacinto and San Andreas faults (Figure 7).

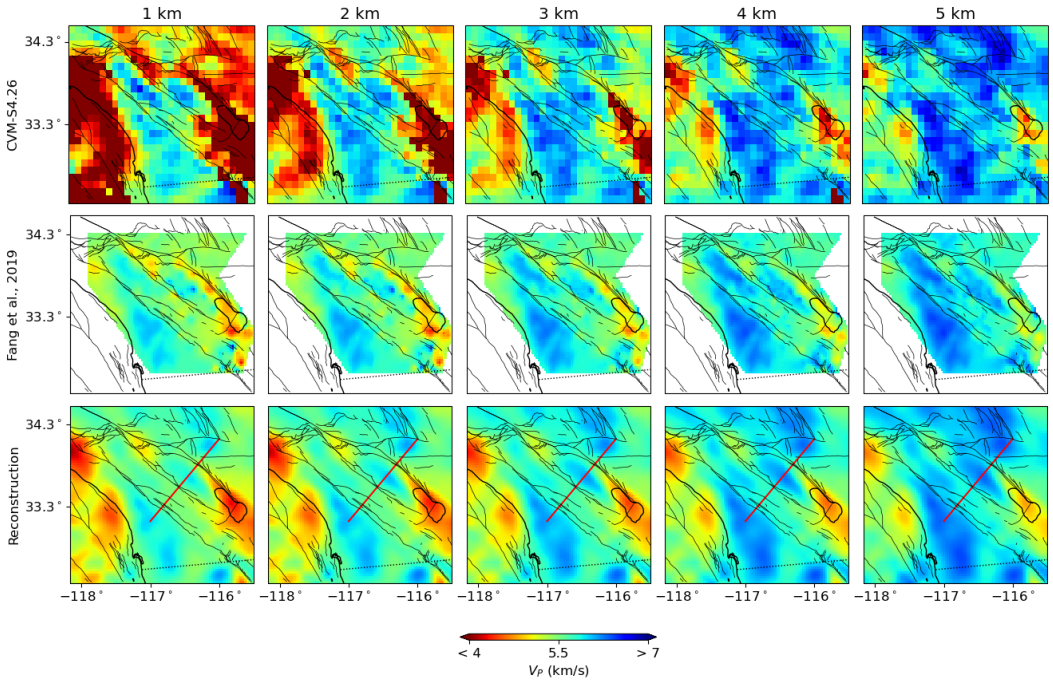

Figure 4. Horizontal slices of V_P at 1, 2, 3, 4, and 5 km depths from CVM-S4.26 (top row), F2019 model (middle row) and the reconstructed model (bottom row). Black lines show major fault traces, as well as the Salton Sea. The red line at the bottom row shows the vertical cross section shown in Figure 7.

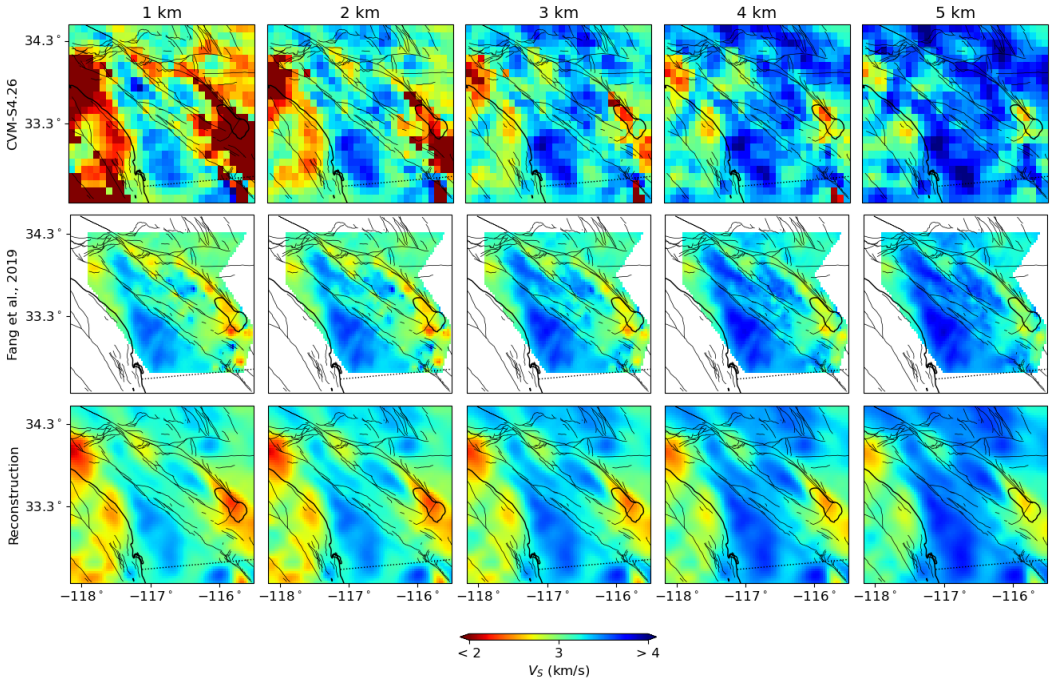

Figure 5. Same as Figure 4 for V_S.

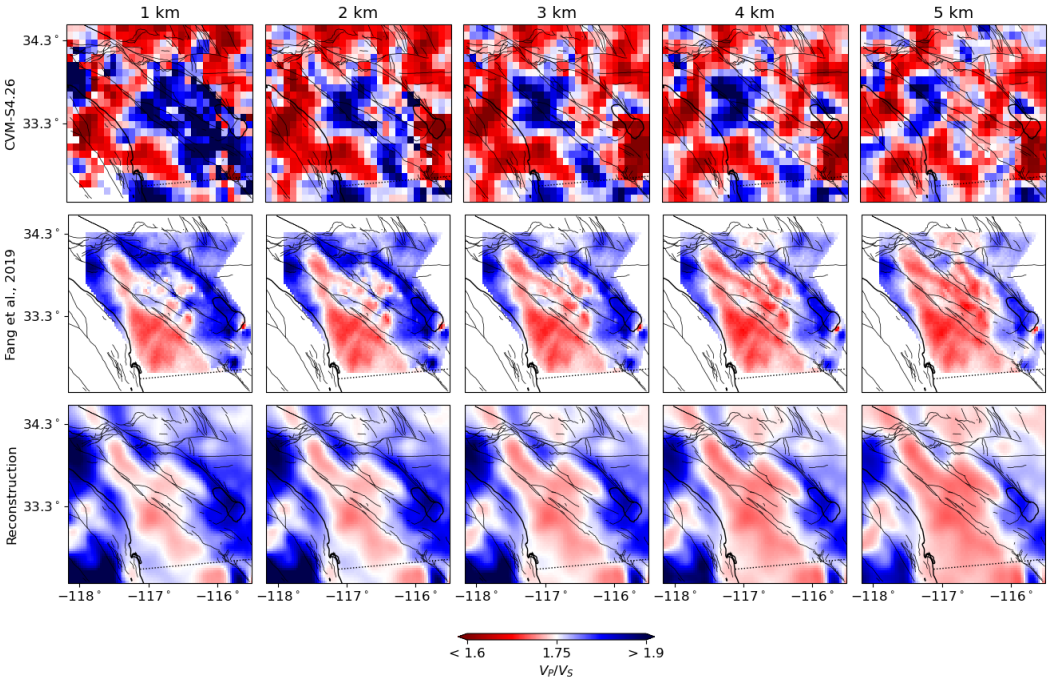

Figure 6. Same as Figure 4 for V_P/V_S.

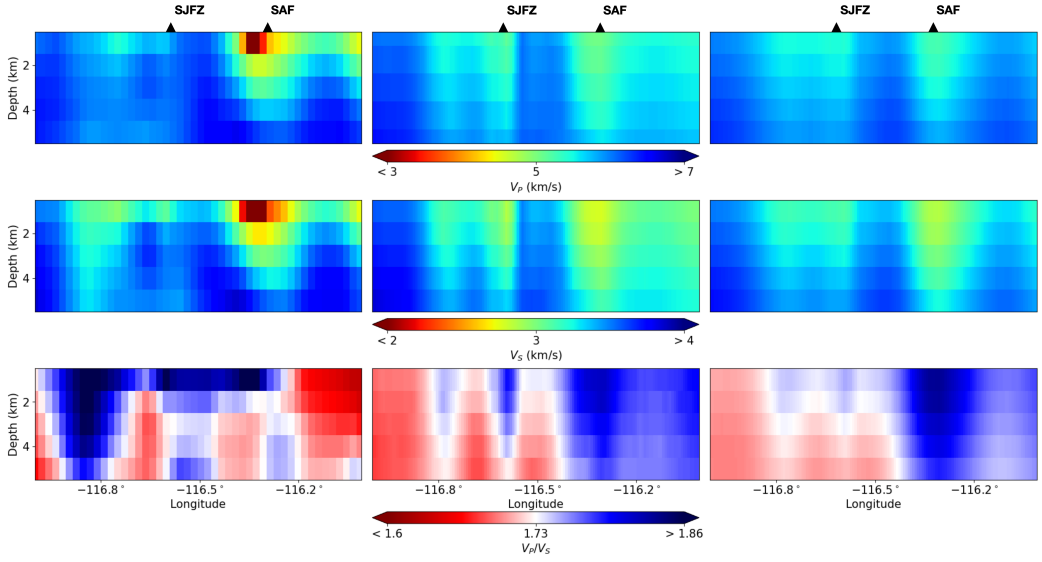

Figure 7. Vertical profiles of V_P (top row), V_S (middle row) and V_P/V_S (bottom row) along the cross-section indicated in Figure 4 in CVM-S4.26 (first column), F2019 model (second column) and the reconstructed model (third column). The locations of the San Andreas Fault (SAF) and San Jacinto Fault Zone (SJFZ) are marked by black triangles.

4 Discussion

We present a method based on sparse dictionary learning for developing transformations between seismic velocity models of different resolutions. The developed technique is used to merge local high-resolution tomographic results within a larger scale lower-resolution model, while simultaneously enhancing the information in the larger scale model. The method is illustrated using V_P, V_S, and V_P/V_S tomographic results of local and regional velocity models in Southern California. The utilized sparse dictionary learning is amenable to interpretation and generalizations. Reconstructed 2D slices and 3D volumes of the regional CVM-S4.26 model (Lee et al., 2014) exhibit visual enhancements and resemblance to results of local higher-resolution target models (Zigone et al., 2015; Fang et al., 2019), which are especially clear for V_P/V_S ratios. The superiority of the reconstructed regional model relative to the original version is demonstrated further below by examining correlations of results with geological features and model validation with numerical simulations of seismic waveforms.

4.1 Interpretability of the dictionary-based method

Sparse dictionary learning is a highly interpretable approach that produces a set of fundamental atoms that can be visualized, and the sparse representation can itself be physically meaningful. For instance, we can define the dominant atom $\boldsymbol{d}_m$ for a given patch $\boldsymbol{p}_j$ as the atom with the largest coefficient in the sparse representation of the patch, i.e., $c_{m,j} = \max(c_{i,j})$, and assign the index of the dominant atom (m) to the center location of the patch. This procedure may be used to classify different regions and obtain a map of dominant atoms distribution which can be further analyzed.

To illustrate, we compare the distribution of the dominant atoms in the results of section 3.3 with velocity profiles and geological features (Figure 8). Patches from areas with low V_P, V_S and high V_P/V_S ratios, such as the north end of SJFZ and around the SAF, mostly have the first atom as the dominant one (red colored in Figure 8)a). To investigate the relationship between atoms and subsurface structures, a cluster analysis is performed on vertical velocity profiles (each profile contains V_P and V_S values over the 1-5 km depth section at a given latitude and longitude) from the F2019 model. The profiles are partitioned into six sets using a K-means algorithm that minimize the inter-cluster variance (Eymold & Jordan, 2019). The spatial distribution of the dominant atoms is correlated with the clusters of seismic velocity profiles; e.g., the green colored area in Figure 8b is consistent with the spatial distribution of first-atom-dominated patches. In addition, the distribution of the dominant atoms is well correlated with the geological map (Figure 8c). The results indicate that the spatial distribution of the first atoms has important information on the geological units and seismic velocities at depth.

Comparing the distribution of the first-atom-dominated patches with the geological map (Figure 8c) shows that it is highly consistent with the distribution of the surface rocks. This consistency further indicates that the surface geological features and rock types are related to the velocity structure at the examined 1-5 km depth sections. The physical interpretability of dictionary learning can thus facilitate establishing correlations between regions in the reconstructed velocity models and geological features.

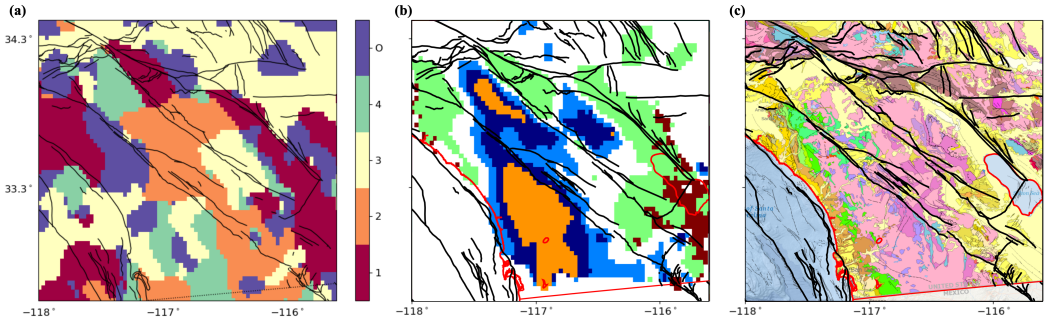

Figure 8. **(a)** Indexes of the dominant atom for the F2019 model in section 3.3. Location of first-atom-dominated patches are colored by dark red. All atoms other than atoms 1-4 are represented by O. **(b)** Clustering of velocity profiles by the K-means algorithm. The cluster corresponding to first-atom-dominated patches is green colored. **(c)** A geological map for Southern California extracted from the website of the California Geological Survey (see Data Availability). The main rock types in the study region are: Continental sedimentary rocks (light yellow), plutonic rocks (pink) and metavolcanic rocks (green).

4.2 Validation of the reconstructed model

To demonstrate further the utility of the presented method, we compare waveform simulation results using the reconstructed model and CVM-S4.26 for a test earthquake (Figure 9a). The hypocentre location of this M4.4 event (Event ID: 38245496) is taken from the relocated catalog of Hauksson et al. (2012, extended to later years) and the moment tensor solution used in the simulation is taken from the catalog of Wang and Zhan (2020). The reconstructed model used in this simulation is obtained by transforming the top 10 km of CVM-S4.26 to the F2019 model using the same dictionary learning approach described in section 3.3. To have a more representative comparison, we also interpolate the top 10 km of CVM-S4.26 to the same resolution as F2019 and refer to this as a baseline model. Since the first layer of both the reconstructed and baseline models are at 1 km depth, we extract the surface velocities from CVM-S4.26 and add them on top of both models. As in Lu and Ben-Zion (2022), the surface topography is implemented by deforming the mesh grid in the vertical direction. Since the F2019 model only provides seismic velocities, we approximate the density (ρ) and quality factors (Q_P, Q_S) using empirical results from (Brocher, 2005) and (Taborda et al., 2016).

The simulations use the SPECFEM3D code (Komatitsch & Tromp, 2002) to compute synthetic waveforms at 3 stations (CI.HEC, CI.BBR, and CI.IKP). The simulation domain is centered at coordinates $(116.53°W, 33.64°N)$ and has a lateral dimension of 320 km $\times$ 280 km in the local Cartesian coordinate (Li et al., 2022). The number of spectral elements along both x and y is 256, making the simulation domain as dense as the grid of the CVM-S4.26 and reconstructed models. We compare observed waveforms and synthetic waveforms in the period band of 0.4-2 Hz, which allows us to focus on the depth range of the enhanced velocity model. As demonstrated in Figure 9, the simulation results based on the reconstructed model exhibit a closer fit to the observations than those produced using the baseline model for both the body waves and surface waves portions of the seismograms. This improvement

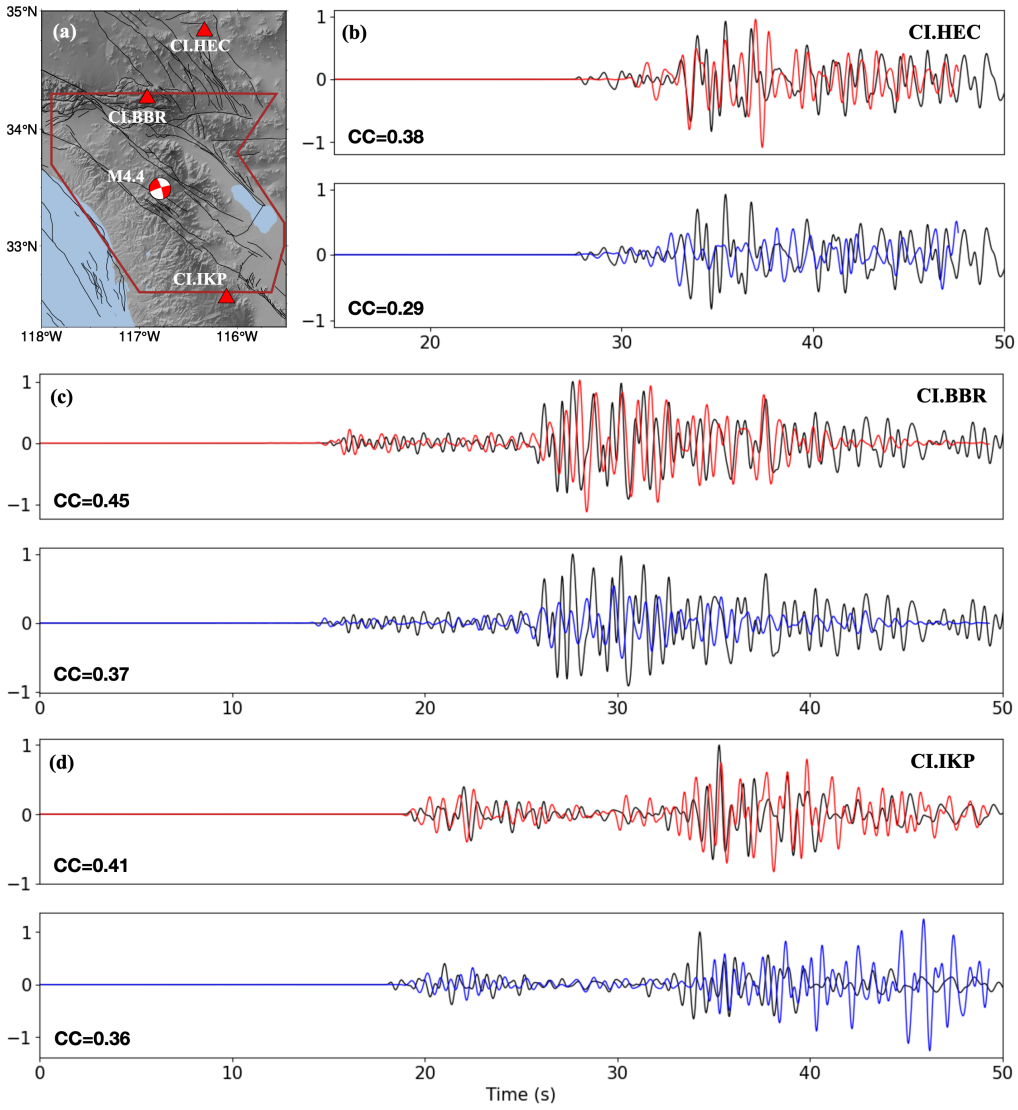

Figure 9. **(a)** Locations of the event and stations (CI.HEC, CI.BBR, and CI.IKP) used for validation. Black lines show major fault traces. The red polygon represents the coverage of the F2019 model. **(b-d)** Vertical components of observational (black lines) and synthetic waveforms at station CI.HEC (b), CI.BBR (c), and CI.IKP (d). The synthetic waveforms are computed for both the reconstructed model (red lines) and the baseline model (CVM-S4.26, blue lines). The CC between observations and simulations are denoted on the bottom-left corner of each panel. All waveforms are bandpass filtered from 0.4 to 2 Hz normalized and by the maximum amplitude of the observed waveform.

is also supported by an increase in the CC between the synthetic and observed waveforms and it exists also for stations outside the common region. The close fit of the simulated amplitude of multiple phases to data indicates that the reconstructed model can improve predictions of earthquake ground motion.

4.3 Limitatioins and outlook for future research

The developed sparse dictionary learning method for transferring high-resolution seismic velocity results to lower velocity models is shown to be effective, but it has several limitations. First, the method requires a local seismic velocity model of high quality, which may not always be available. Furthermore, factors such as overall consistency between the regional and local models, as well as the resolution, coverage, and geological features in the data utilized, can influence the quality of the trained dictionaries and the reconstructed models. Additionally, the selection of hyper-parameters (section 2.2) may vary for different models and should be tuned through experimentation and validation. In the present work we aimed primarily to develop and illustrate the method, and have conducted only example waveform simulations for validation. A future study will include a more comprehensive validation using multiple earthquakes, virtual seismic noise sources, and many stations.

The developed method for merging and enhancing velocity models can be applied to other regions that have well-developed regional seismic velocity models and local high quality models, such as northern California, Europe and Japan. The improved multi-scale velocity models can have numerous applications in the field of seismology. Examples include more accurate derivation of earthquake source properties and more realistic simulations of ground motion over a wider range of frequencies leading to better estimates of seismic hazard. The concept of dictionary representation and transformation presented in this paper can be applied to additional earth science datasets. For instance, high-resolution surface deformation observed from InSAR is limited to areas with high correlations not including, for example, highly vegetated regions (e.g. Wei & Sandwell, 2010). An approach similar to the one developed in this paper can enhance regional low-resolution deformation observations with higher-resolution local results. Furthermore, the low temporal resolution of InSAR data can be improved by high temporal resolution GPS data regarding the timeline as an extra dimension (e.g. Xu et al., 2022). The interpretability of the dictionary learning method can also allow discovering spatial and temporal correlations between different physical quantities, such as geological features, seismic velocity structure and surface deformation.

Data Availability

The CVM-S4.26 model is available on the UCVM software provided by the Southern California Earthquake Center (`https://www.scec.org/software/ucvm`). Other seismic velocity models used in this study are from Zigone et al. (2015) and Fang et al. (2019). The earthquake waveform data used in this paper is retrieved from the data center of the southern California network CI (`https://scedc.caltech.edu/data`). The geological data in Figure 8 were obtained from the CGS website (`https://maps.conservation.ca.gov/cgs/gmc/`).

Acknowledgments

We thank Guoliang Li for help with the waveform simulations. This research is supported by the U.S. Department of Energy (Award DE-SC0016520).

References

Ajala, R., & Persaud, P. (2021). Effect of Merging Multiscale Models on Seismic Wavefield Predictions Near the Southern San Andreas Fault. *Journal of Geophysical Research: Solid Earth*, *126*(10), e2021JB021915. doi: doi:10.1029/2021JB021915

Allam, A. A., & Ben-Zion, Y. (2012). Seismic velocity structures in the southern California plate-boundary environment from double-difference tomography. *Geophysical Journal International*, *190*(2), 1181-1196. doi: doi:10.1111/j.1365-246X.2012.05544.x

Beckouche, S., & Ma, J. (2014). Simultaneous dictionary learning and denoising for seismic data. *GEOPHYSICS*, *79*(3), A27-A31. doi: doi:10.1190/geo2013-0382.1

Bianco, M. J., & Gerstoft, P. (2018). Travel time tomography with adaptive dictionaries. *IEEE Transactions on Computational Imaging*, *4*(4), 499-511. doi: doi:10.1109/TCI.2018.2862644

Bonilla, L. F., Steidl, J. H., Gariel, J.-C., & Archuleta, R. J. (2002). Borehole Response Studies at the Garner Valley Downhole Array, Southern California. *Bulletin of the Seismological Society of America*, *92*(8), 3165-3179. doi: doi:10.1785/0120010235

Brocher, T. M. (2005). Empirical Relations between Elastic Wavespeeds and Density in the Earth's Crust. *Bulletin of the Seismological Society of America*, *95*(6), 2081–2092. doi: doi:10.1785/0120050077

Dong, C., Loy, C. C., He, K., & Tang, X. (2015). *Image super-resolution using deep convolutional networks.* arXiv. doi: doi:10.48550/ARXIV.1501.00092

Eymold, W. K., & Jordan, T. H. (2019). Tectonic Regionalization of the Southern California Crust From Tomographic Cluster Analysis. *Journal of Geophysical Research: Solid Earth*, *124*(11), 11840–11865. doi: doi:10.1029/2019JB018423

Fang, H., White, M. C. A., Lu, Y., & Ben-Zion, Y. (2022). Seismic traveltime tomography of southern california using poisson-voronoi cells and 20 years of data. *Journal of Geophysical Research: Solid Earth*, *127*(5), e2021JB023307. doi: doi:10.1029/2021JB023307

Fang, H., Yao, H., Zhang, H., Thurber, C., Ben-Zion, Y., & van der Hilst, R. D. (2019). Vp/Vs tomography in the southern California plate boundary region using body and surface wave traveltime data. *Geophysical Journal International*, *216*(1), 609–620. doi: doi:10.1093/gji/ggy458

Fichtner, A., van Herwaarden, D.-P., Afanasiev, M., Simutė, S., Krischer, L., Çubuk Sabuncu, Y., ... Igel, H. (2018). The Collaborative Seismic Earth Model: Generation 1. *Geophysical Research Letters*, *45*(9), 4007–4016. doi: doi:10.1029/2018GL077338

Gatys, L. A., Ecker, A. S., & Bethge, M. (2016, June). Image style transfer using convolutional neural networks. In *Proceedings of the ieee conference on computer vision and pattern recognition (cvpr).*

Gibbs, J. F., Boore, D. M., Tinsley III, J. C., & Mueller, C. S. (2001). *Borehole P- and S-wave velocity at thirteen stations in Southern California* (Report No. 2001-506). Reston, VA. doi: doi:10.3133/ofr01506

Hauksson, E., Yang, W., & Shearer, P. M. (2012). Waveform Relocated Earthquake Catalog for Southern California (1981 to June 2011). *Bulletin of the Seismological Society of America*, *102*(5), 2239–2244. doi: doi:10.1785/0120120010

Hillers, G., Roux, P., Campillo, M., & Ben-Zion, Y. (2016). Focal spot imaging based on zero lag cross-correlation amplitude fields: Application to dense array data at the san jacinto fault zone. *Journal of Geophysical Research: Solid Earth*, *121*(11). doi: doi:10.1002/2016JB013014

Juarez, A., & Ben-Zion, Y. (2020). Effects of Shallow-Velocity Reductions on 3D Prop-

agation of Seismic Waves. *Seismological Research Letters*, *91*(6), 3313–3322. doi: doi:10.1785/0220200183

Komatitsch, D., & Tromp, J. (2002). Spectral-element simulations of global seismic wave propagation—I. Validation. *Geophysical Journal International*, *149*(2), 390–412. doi: doi:10.1046/j.1365-246X.2002.01653.x

Kreutz-Delgado, K., Murray, J. F., Rao, B. D., Engan, K., Lee, T.-W., & Sejnowski, T. J. (2003). Dictionary Learning Algorithms for Sparse Representation. *Neural Computation*, *15*(2), 349–396. doi: doi:10.1162/089976603762552951

Lee, E.-J., Chen, P., Jordan, T. H., Maechling, P. B., Denolle, M. A. M., & Beroza, G. C. (2014). Full-3-d tomography for crustal structure in southern california based on the scattering-integral and the adjoint-wavefield methods. *Journal of Geophysical Research: Solid Earth*, *119*(8), 6421-6451. doi: doi:10.1002/2014JB011346

Li, G., Tao, K., Chen, M., Li, J., Maguire, R., & Ma, X. (2022). Cartesian Meshing Spherical Earth (CMSE): A Code Package to Incorporate the Spherical Earth in SPECFEM3D Cartesian Simulations. *Seismological Research Letters*, *93*(2A), 986-996. doi: doi:10.1785/0220210131

Lu, Y., & Ben-Zion, Y. (2022). Validation of seismic velocity models in southern California with full-waveform simulations. *Geophysical Journal International*, *229*(2), 1232–1254. doi: doi:10.1093/gji/ggab534

Mairal, J., Bach, F., Ponce, J., & Sapiro, G. (2009). Online dictionary learning for sparse coding. In *Proceedings of the 26th annual international conference on machine learning* (pp. 689–696).

Mallat, S., & Zhang, Z. (1993). Matching pursuits with time-frequency dictionaries. *IEEE Transactions on Signal Processing*, *41*(12). doi: doi:10.1109/78.258082

Mordret, A., Roux, P., Boué, P., & Ben-Zion, Y. (2019). Shallow three-dimensional structure of the San Jacinto fault zone revealed from ambient noise imaging with a dense seismic array. *Geophysical Journal International*, *216*(2), 896-905. doi: doi:10.1093/gji/ggy464

Rubinstein, R., Bruckstein, A. M., & Elad, M. (2010). Dictionaries for Sparse Representation Modeling. *Proceedings of the IEEE*, *98*(6), 1045–1057. doi: doi:10.1109/JPROC.2010.2040551

Share, P.-E., Allam, A. A., Ben-Zion, Y., Lin, F.-C., & Vernon, F. L. (2019). Structural Properties of the San Jacinto Fault Zone at Blackburn Saddle from Seismic Data of a Dense Linear Array. *Pure and Applied Geophysics*, *176*(3), 1169–1191. doi: doi:10.1007/s00024-018-1988-5

Shaw, J. H., Plesch, A., Tape, C., Suess, M. P., Jordan, T. H., Ely, G., ... Munster, J. (2015). Unified structural representation of the southern california crust and upper mantle. *Earth and Planetary Science Letters*, *415*, 1-15. doi: doi:10.1016/j.epsl.2015.01.016

Sulam, J., You, C., & Zhu, Z. (2020). *Recovery and Generalization in Over-Realized Dictionary Learning.* Retrieved from http://arxiv.org/abs/2006.06179 doi: doi:10.48550/arXiv.2006.06179

Taborda, R., Azizzadeh-Roodpish, S., Khoshnevis, N., & Cheng, K. (2016). Evaluation of the southern California seismic velocity models through simulation of recorded events. *Geophysical Journal International*, *205*(3), 1342–1364. doi: doi:10.1093/gji/ggw085

Tibshirani, R. (1996). Regression Shrinkage and Selection via the Lasso. *Journal of the Royal Statistical Society. Series B (Methodological)*, *58*(1), 267–288.

Wang, X., & Zhan, Z. (2020). Moving from 1-D to 3-D velocity model: automated waveform-

based earthquake moment tensor inversion in the Los Angeles region. *Geophysical Journal International*, *220*(1), 218-234. doi: doi:10.1093/gji/ggz435

Wei, M., & Sandwell, D. T. (2010). Decorrelation of l-band and c-band interferometry over vegetated areas in california. *IEEE Transactions on Geoscience and Remote Sensing*, *48*(7), 2942-2952. doi: doi:10.1109/TGRS.2010.2043442

Xu, X., Hua, R., & Guns, K. A. (2022). Predicting InSAR deformation with GNSS using machine learning. In *AGU fall meeting abstracts* (Vol. 2022, p. G45A-01).

Yang, J., Wright, J., Huang, T., & Ma, Y. (2008). Image super-resolution as sparse representation of raw image patches. In *2008 ieee conference on computer vision and pattern recognition* (p. 1-8). doi: doi:10.1109/CVPR.2008.4587647

Yeh, T.-Y., & Olsen, K. B. (2022). Data-constrained fault zone structure improves 0-3 Hz deterministic ground motion predictions for the 2019 M7.1 Ridgecrest earthquake. In *Poster Presentation at 2022 SCEC Annual Meeting.*

Zigone, D., Ben-Zion, Y., Campillo, M., & Roux, P. (2015). Seismic Tomography of the Southern California Plate Boundary Region from Noise-Based Rayleigh and Love Waves. *Pure and Applied Geophysics*, *172*(5), 1007–1032. doi: doi:10.1007/s00024-014-0872-1

Enhancing regional seismic velocity model with higher-resolution local results using sparse dictionary learning

Hao Zhang[1] **and Yehuda Ben-Zion**[1,2]

[1]Department of Earth Sciences, University of Southern California, Los Angeles, California, USA
[2]Southern California Earthquake Center, University of Southern California, Los Angeles, California, USA

Key Points:

- We present a new method for merging multi-scale velocity models with different resolutions.
- We reconstruct a high resolution regional seismic velocity model for southern California.
- Validation with waveform simulations shows that the reconstructed model outperforms the original model.

Corresponding author: Hao Zhang, hzhang63@usc.edu

Abstract

We use sparse dictionary learning to develop transformations between seismic velocity models of different resolution and spatial extent. Starting with results in the common region of both models, the method can be used to enhance a regional lower-resolution model to match the style and resolution of local higher-resolution results while preserving its regional coverage. The method is demonstrated by applying it to two-dimensional V_s and three-dimensional V_P and V_S local and regional velocity models in southern California. The enhanced reconstructed models exhibit clear visual improvements, especially in the reconstructed V_P/V_S ratios, and better correlations with geological features. We demonstrate the improvements of the reconstructed model relative to the original velocity model by comparing waveform simulation results to observations. The improved fitting to observed waveforms extends beyond the domain of the overlapping region. The developed dictionary learning approach provides physically interpretable results and offers a powerful tool for additional applications for data enhancement in earth sciences.

Plain Language Summary

Seismic velocity models are essential for many applications including derivation of earthquake properties, studies of tectonic processes, and analysis of earthquake ground motions. In various places there are velocity models of different spatial coverage and resolution. To benefit from the complementary strengths of such models, we develop a new method for enhancing regional velocity models of relatively low-resolution with information contained in local higher-resolution models. The method builds a transformation between different models in their common local region based on a sparse dictionary learning and then uses the transformation outside the common region. We apply the method to seismic velocity models in southern California and show that the enhanced regional model outperforms the original velocity model in fitting earthquake waveforms and also has better consistency with geological features. The method has a potential for improving the quality of other data sets in earth science.

1 Introduction

Seismic velocity models are foundational to numerous applications including derivations of earthquake source properties, simulations of seismic ground motion from scenario earthquakes, and a broad range of structural and tectonophysics topics. The spatial coverage and resolution of derived velocity models depend on the data and inversion methods used, and models of widely different scales and resolutions are often available in well-studied regions. In southern California, there are several regional velocity models with a nominal resolution of about 5 km (e.g. Lee et al., 2014; Shaw et al., 2015; Fang et al., 2022), along with models focusing on the San Jacinto and San Andreas faults with a nominal resolution of 2-3 km (e.g. Allam & Ben-Zion, 2012; Zigone et al., 2015; Fang et al., 2019; Share et al., 2019). More local models based on dense array data can have resolution approaching tens of meters (e.g. Hillers et al., 2016; Mordret et al., 2019) and results based on borehole data can resolve sub-cm features (e.g. Gibbs et al., 2001; Bonilla et al., 2002). Developing methods to merge velocity models of different scales and resolutions can provide multi-scale frameworks that benefit from the complementary strengths of the different results.

The most straightforward approach to combine models is to embed small-scale high-resolution velocity models within regional models and smooth the boundaries (e.g. Fichtner et al., 2018; Ajala & Persaud, 2021). While this approach is simple, the obtained seismic velocities near the boundaries between models depend on ad-hoc choices of the applied smoothing parameters. Importantly, local perturbations to seismic wavefields generated near the boundaries between models can affect the seismic wavefield on a regional scale (e.g. Juarez & Ben-Zion, 2020; Ajala & Persaud, 2021; Yeh & Olsen, 2022). Furthermore, embedding only updates the low-resolution model in the area covered by the high-resolution results, without enhancing the outer region, and such procedures disregard useful information from the low-resolution results in the area covered by the high-resolution model. In the present study we develop a method for merging multi-scale velocity models by establishing a transformation between models of different resolutions. Specifically, we develop a transformation by comparing high- and low- resolution imaging results in a given region and then utilize this transformation to enhance the low-resolution model both in the overlapping region as well as outside it.

The developed methodology is inspired by progress made in machine learning algorithms for super-resolution (Dong et al., 2015) and style transfer (Gatys et al., 2016) of images. To merge seismic velocity models, we use a data-driven approach based on sparse dictionary learning (Yang et al., 2008; Mairal et al., 2009). Since the available amount of data is limited, we opt for this approach over Convolutional Neural Networks (CNN) that demand a large number of trainable parameters. Dictionary learning involves a linear decomposition of an input signal utilizing a small set of basis signals, referred to as atoms, which are learned from the data. This technique has achieved impressive outcomes in various image and video processing tasks. In seismology, dictionary learning was used for signal denoising (Beckouche & Ma, 2014) and for seismic tomography (Bianco & Gerstoft, 2018). Dictionary learning has the added benefits of being physically interpretable (in contrast to CNN), and better generalization capability than CNN when the dataset is limited (Sulam et al., 2020).

In the following sections, we first introduce a framework for representing seismic velocity models using dictionaries and subsequently devise a method for developing a transformation between models that can enrich the lower-resolution model. As initial applications, we implement the technique on both 2D and 3D velocity models in southern California with different resolution and spatial extent. We generate an enhanced reconstructed version of the regional community velocity model CVM-S4.26 (Lee et al., 2014) utilizing a higher-resolution model around the San Jacinto fault zone (Fang et al., 2019), and demonstrate by comparing waveform simulations with observations that the reconstructed model outperforms the original version.

2 Methods

2.1 Dictionary representation of velocity models

Dictionary Learning involves identifying a sparse representation of input data in the form of a linear combination of basis atoms inferred from the input data (Mairal et al., 2009), and it provided important results in compressed sensing and signal recovery. In this section, we present a novel method for applications on merging and enhancing seismic velocity models.

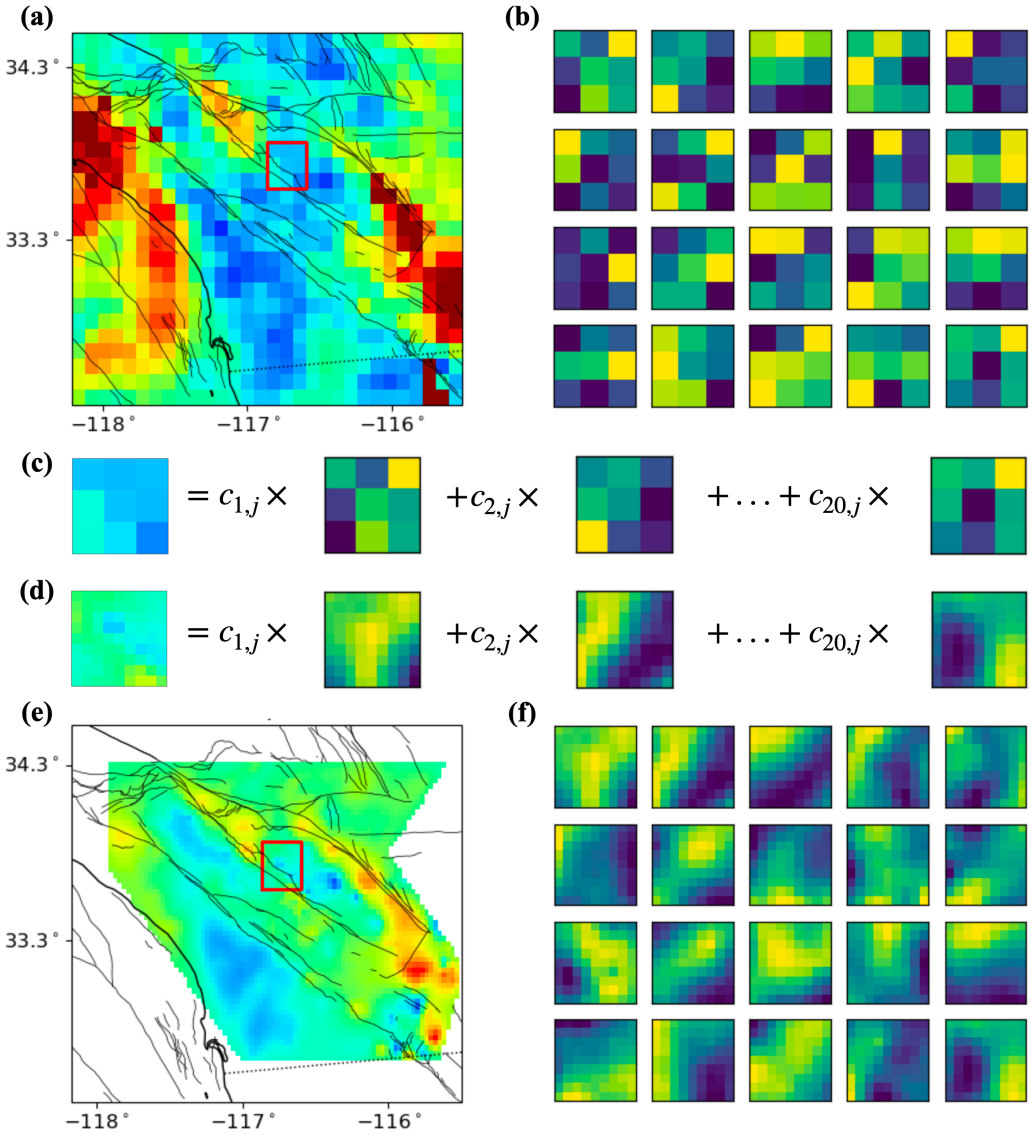

Figure 1. Dictionary representation of seismic velocity models and transformation between them. **(a)** Horizontal slice of CVM-S4.26 at 2 km depth with a resolution of $0.09° \times 0.09°$. The red square indicates the patch used in (c). **(b)** A dictionary consisting of 20 atoms learned from the velocity model in (a). **(c)** Each patch extracted from the velocity model can be represented as a linear superposition of atoms in the dictionary. **(d)** The patch extracted from the model in (e) at the same location can be represented using another dictionary with the same sparse representation. **(e)** Horizontal slice of the Fang et al. (2019) model in the same region as (a) but with higher-resolution. **(f)** A dictionary learned from the velocity model in (e). All atoms are reshaped to the window size for better visualization.

Seismic velocity models are represented as 2D or 3D grids that contain information about P wave velocity V_P and/or S wave velocity V_S at a set of specific spatial locations. Given a seismic velocity model $\mathcal{M}$, we can utilize a sliding window which has the same dimension as the model to extract patches from it, resulting in N patches $\boldsymbol{p}_1, ..., \boldsymbol{p}_N$ that represent values inside subsections of the model (Figure 1a). To simplify the description, we flatten each patch into a 1D array with length L representing the number of grids within the window (Dong et al., 2015). For example, $L = 9$ if the size of a 2D window is 3×3, and $L = 90$ if the window is a $3 \times 3 \times 10$ cube. The set of flattened patches is denoted as $\mathbf{P} \in \mathbb{R}^{L \times N}$.

The dictionary representation of the seismic velocity model is used to find a linear relationship among the patches in $\mathbf{P}$ and their low-dimensional projections, i.e., a dictionary $\mathbf{D}^* = [\boldsymbol{d}_1, ..., \boldsymbol{d}_K] \in \mathbb{R}^{L \times K}$ contains K prototype atoms (with $K < N$ usually), each with the same length as the patches (Figure 1b). Each patch $\boldsymbol{p}_j \in \mathbb{R}^L$ can be represented as a sparse linear combination of the atoms in $\mathbf{D}^*$:

$$\boldsymbol{p}_j \approx \mathbf{D}^* \boldsymbol{c}_j = \sum_{i=1}^{K} c_{i,j} \boldsymbol{d}_i, \tag{1}$$

where $\boldsymbol{c}_j = [c_{1,j}, ..., c_{K,j}]^T$ and $c_{i,j}$ and $c_{i,j}$ represents the sparse coefficients for patches $\boldsymbol{p}_j$ for atoms $\boldsymbol{d}_i$ (Figure 1c). These linear combinations can be written in a matrix form as

$$\mathbf{P} \approx \mathbf{D}^* \mathbf{C}^*, \tag{2}$$

where $\mathbf{C}^* = [\boldsymbol{c}_1, ..., \boldsymbol{c}_N] \in \mathbb{R}^{K \times N}$ is the sparse representation matrix with very few nonzero entries (Kreutz-Delgado et al., 2003).

To solve the dictionary $\mathbf{D}^*$ and coefficients $\mathbf{C}^*$ from patches, we use a sparse coding algorithm (e.g. Rubinstein et al., 2010) that seeks to minimize the difference between the patches and the reconstruction from linear superposition

$$\mathbf{D}^*, \mathbf{C}^* = \underset{\mathbf{D},\mathbf{C}}{\operatorname{argmin}} \|\mathbf{P} - \mathbf{D}\mathbf{C}\|_2^2 + \lambda \|\mathbf{C}\|_0. \tag{3}$$

where $\|\cdot\|_2$ and $\|\cdot\|_0$ are the second and zero order norm, respectively. The regularization parameter λ controls the tradeoff between the sparsity and the minimization error. Various algorithms, such as Orthogonal Matching Pursuit (OMP) (Mallat & Zhang, 1993) and Least Absolute Shrinkage and Selection Operator (LASSO) Tibshirani (1996), can be used to solve this optimization problem (3). After obtaining the dictionary $\mathbf{D}^*$ and corresponding representation matrix $\mathbf{C}^*$ using the sparse coding algorithm, the reconstructed patches is calculated as $\hat{\mathbf{P}} = \mathbf{D}^*\mathbf{C}^*$. The updated velocity model can be then developed by stitching the reconstructed patches together in their original spatial order (Dong et al., 2015).

2.2 Transformation between two seismic velocity models

The dictionary representation technique can facilitate the transformation between two different seismic velocity models by establishing a correspondence between their respective dictionaries. Suppose we have an initial model $\mathcal{M}_1$ and a second more local model $\mathcal{M}_2$ with a higher-resolution that is spatially included in $\mathcal{M}_1$ (Figure 1a,e). Our goal is to transform $\mathcal{M}_1$ to model $\hat{\mathcal{M}}$, with resolution and values in the common region of both models consistent with $\mathcal{M}_2$ and enhanced resolution outside the overlapping region. Essentially, this transformation should improve $\mathcal{M}_1$ to match the resolution and style of $\mathcal{M}_2$ while preserving its coverage.

To solve the problem described above, we divide it into three steps. In the first step, we extract patches $\mathbf{P}_1^{\mathrm{U}} = [\boldsymbol{p}_1^1, ..., \boldsymbol{p}_1^{N_1}] \in \mathbb{R}^{L_1 \times N_1}$ from the entire $\mathcal{M}_1$. A subset of $\mathbf{P}_1^{\mathrm{U}}$, $\mathbf{P}_1 = [\boldsymbol{p}_1^1, ..., \boldsymbol{p}_1^{N_2}] \in \mathbb{R}^{L_1 \times N_2}$ shares spatial locations with patches $\mathbf{P}_2 = [\boldsymbol{p}_2^1, ..., \boldsymbol{p}_2^{N_2}] \in \mathbb{R}^{L_1 \times N_2}$ extracted from $\mathcal{M}_2$. Such pairs of patches, e.g., $\boldsymbol{p}_1^i$ and $\boldsymbol{p}_2^i$, extracted from the same spatial locations are aligned by their index in $\mathbf{P}_1$ and $\mathbf{P}_2$. The length of the patches, L_1 and L_2, may differ due to the different resolution of $\mathcal{M}_1$ and $\mathcal{M}_2$. In the second step, we transfer the patches from $\mathbf{P}_1^{\mathrm{U}}$ to $\hat{\mathbf{P}}$ to ensure that under this transformation the transformed $\mathbf{P}_1$ is consistent with $\mathbf{P}_2$. Finally, the transformed patches $\hat{\mathbf{P}}$ are put back to their original spatial location to rebuild the transformed velocity model $\hat{\mathcal{M}}$.

The dictionary representation technique described in section 2.1 is applied in the second step, i.e., the transformation of patches from $\mathbf{P}_1^{\mathrm{U}}$ to $\hat{\mathbf{P}}$. First, we represent patches in $\mathbf{P}_1$ as sparse linear combination of K atoms in a dictionary $\mathbf{D}_1 = [\boldsymbol{d}_1^1, ..., \boldsymbol{d}_1^K] \in \mathbb{R}^{L_1 \times K}$

$$\mathbf{P}_1 \approx \mathbf{D}_1 \mathbf{C}. \tag{4}$$

This produces a sparse representation $\mathbf{C} \in \mathbb{R}^{K \times N_2}$ that contains the sparse coefficients for each patch in $\mathbf{P}_1$ (Figure 1c). The dictionary $\mathbf{D}_1$ and the sparse representation $\mathbf{C}$ can be obtained simultaneously using sparse coding algorithms (section 2.1). We also represent the patches in $\mathbf{P}_2$ as a linear combination of atoms in a second (higher-resolution) dictionary $\mathbf{D}_2 = [\boldsymbol{d}_2^1, ..., \boldsymbol{d}_2^K] \in \mathbb{R}^{L_2 \times K}$ with the same sparse representation $\mathbf{C}$ (Figure 1d,f)

$$\mathbf{P}_2 \approx \mathbf{D}_2 \mathbf{C}. \tag{5}$$

The atom $\boldsymbol{d}_2^j$ in $\mathbf{D}_2$ have one-to-one corresponding to $\boldsymbol{d}_1^j$ in $\mathbf{D}_1$ due to the duality between $\mathbf{P}_1$ and $\mathbf{P}_2$. Therefore, we can first represent $\mathbf{P}_1^{\mathrm{U}}$ on $\mathbf{D}_1$ using a representation matrix $\mathbf{C}^{\mathrm{U}}$ and then construct the transferred patches $\hat{\mathbf{P}} = \mathbf{D}_2 \mathbf{C}^{\mathrm{U}}$.

In practice, we randomly divide the patches $\mathbf{P}_1$ and $\mathbf{P}_2$ into training set $\mathbf{P}_1^{\mathrm{T}}$, $\mathbf{P}_2^{\mathrm{T}}$ and validation set $\mathbf{P}_1^{\mathrm{V}}$, $\mathbf{P}_2^{\mathrm{V}}$, and put each pair of patches with the same location in the same dataset. The training set is utilized to learn the dictionary and sparse representation matrix, while the validation set is used to select optimal parameters. We use the OMP algorithm to obtain the dictionary $\mathbf{D}_1$ for the train set $\mathbf{P}_1^{\mathrm{T}}$ and the corresponding sparse representation $\mathbf{C}^{\mathrm{T}}$ from following optimization:

$$\mathbf{D}_1, \mathbf{C}^{\mathrm{T}} = \underset{\mathbf{D},\mathbf{C}}{\operatorname{argmin}} \|\mathbf{P}_1^{\mathrm{T}} - \mathbf{D}\mathbf{C}\|_2^2 + \lambda \|\mathbf{C}\|_0. \tag{6}$$

For the derived sparse representation $\mathbf{C}^{\mathrm{T}}$, we calculate the corresponding dictionary

$$\mathbf{D}_2 = \underset{\mathbf{D}}{\operatorname{argmin}} \|\mathbf{P}_2^{\mathrm{T}} - \mathbf{D}\mathbf{C}^{\mathrm{T}}\|_2^2 \tag{7}$$

from $\mathbf{P}_2^{\mathrm{T}}$ using the Least Squares Method. Then we use the validation set to evaluate the performance of the trained dictionaries $\mathbf{D}_1$ and $\mathbf{D}_2$. The patches in $\mathbf{P}_1^{\mathrm{V}}$ are represented on the trained $\mathbf{D}_1$ using a sparse representation

$$\mathbf{C}^{\mathrm{V}} = \underset{\mathbf{C}}{\operatorname{argmin}} \|\mathbf{P}_1^{\mathrm{V}} - \mathbf{D}_1\mathbf{C}\|_2^2 + \lambda \|\mathbf{C}\|_0. \tag{8}$$

We then compare the difference between the transferred validation set $\hat{\mathbf{P}}^{\mathrm{V}} = \mathbf{D}_2 \mathbf{C}^{\mathrm{V}}$ and $\mathbf{P}_2^{\mathrm{V}}$. The difference between patches $\mathbf{P}$ and the baseline patches $\mathbf{P}_0$ is defined as

$$D(\mathbf{P}, \mathbf{P}_0) = \frac{\|\mathbf{P} - \mathbf{P}_0\|_2}{\|\mathbf{P}_0\|_2}. \tag{9}$$

The optimal hyper-parameters in the training procedure (e.g, the K number of atoms in a dictionary and the sparsity control parameter λ) are found by minimizing the difference $D(\hat{\mathbf{P}}^{\mathrm{V}}, \mathbf{P}_2^{\mathrm{V}})$.

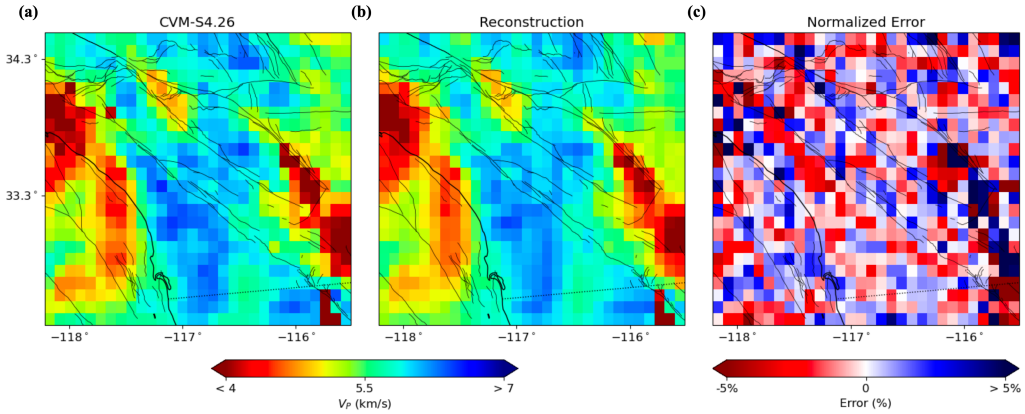

Figure 2. **(a)** Horizontal slice of V_p at 2 km depth from CVM-S4.26. The sampled resolution is $0.09° \times 0.09°$. **(b)** Reconstruction of the model in (a) using a dictionary representation. **(c)** The difference (error) between the reconstruction and the original model normalized at each grid by the value in the original model. Black lines mark major fault traces.

3 Results

3.1 Capability of the dictionary representation

As the basis of our methodology for transforming seismic velocity models, we first demonstrate the capability of representing a seismic velocity model using a dictionary with minimal error. We use a horizontal slice of V_P at 2 km depth from the CVM-S4.26 model (Lee et al., 2014) as an example (Figure 2a). This waveform-based community velocity model for southern California was shown to have a good overall performance in a validation study using waveform simulations (Lu & Ben-Zion, 2022). With a horizontal resolution of $0.09° \times 0.09°$, there are 30 grid points along the longitude direction and 24 grid points along the latitude direction in this horizontal slice.

We extract 616 patches from this model using a sliding window of size 3×3 and a stride (amount of grid points of window's movement over the model in one direction) of 1. In the training of the dictionary using OMP, we set the regularization parameter λ as 0.1 and the number of atoms in the dictionary to be 20 (Figure 1b). The resulting sparse representation of the model in the dictionary is then used to reconstruct the model (Figure 2b). The average error between the reconstruction and the original model is 2.2% while the peak error at a single grid is 7%, demonstrating accurate reconstruction using the dictionary representation. We applied the dictionary representation to other 2D or 3D velocity models utilized in this study and the resulting errors are found to be consistently small.

3.2 Transformation between 2D V_S models

In this section, we evaluate the performance of the method for 2D sections of V_S results. Zigone et al. (2015) derived a 3D V_S model around the San Jacinto and San Andreas faults in Southern California from Rayleigh wave velocities constructed from the ambient seismic noise. The model, referred to below as Z2015 and chosen as the target model $\mathcal{M}_2$, has high-resolution in the top 7 km. As illustrated in Figure 3a with a horizontal slice at a

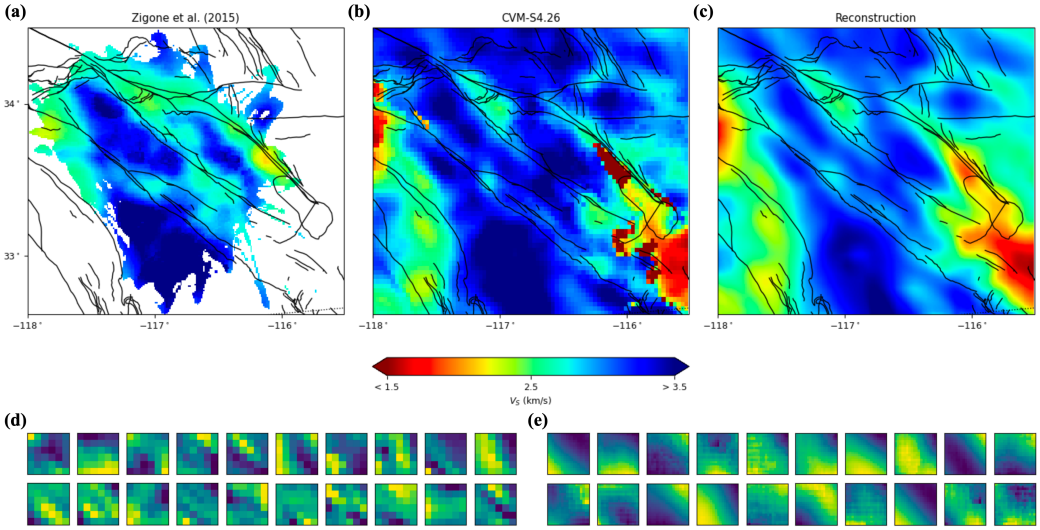

Figure 3. **(a-c)** Horizontal slices of V_S at 2 km depth from the Z2015 model (a), CVM-S4.26 (b), and the reconstructed model (c). The resolution of the Z2015 and reconstructed models is $0.01^\circ \times 0.01^\circ$, while the resolution of CVMS is $0.03^\circ \times 0.03^\circ$. Black lines show major fault traces. **(d)** low-resolution dictionary $\mathbf{D}_1$ and **(e)** high-resolution dictionary $\mathbf{D}_2$ learned from the training data. All atoms are reshaped to the window size for better visualization.

depth of 2 km, the results exhibit informative lateral variations including low velocity zones and velocity contrasts across the main faults. On the other hand, the regional model CVM-S4.26 used as the initial model $\mathcal{M}_1$ shows clearly low velocity sediments in the Salton Trough (Figure 3b), outside the spatial extent of Z2015. The horizontal resolution of $\mathcal{M}_1$ and $\mathcal{M}_2$ are $0.03^\circ \times 0.03^\circ$ and $0.01^\circ \times 0.01^\circ$, respectively, and the range of CVM-S4.26 used in the analysis is larger than that of $\mathcal{M}_2$ (Figures 3a,b).

Patches are extracted from the overlapping area using a 6×6 sliding square window on $\mathcal{M}_1$ with a stride of 1 and a 18×18 sliding window on $\mathcal{M}_2$ with a stride of 3. To have efficient training of dictionaries, we compute the cross-correlation (CC) between upsampled low-resolution patches and their corresponding high-resolution patches. We only utilize patch pairs with $CC > 0$ for both training and validation. Following this selection process, 1131 patch pairs are available for analysis in this example application, from which we randomly select 1000 pairs as the training set $\mathbf{P}_1^{\mathrm{T}}$ and $\mathbf{P}_2^{\mathrm{T}}$, while the remaining pairs are allocated for the validation set $\mathbf{P}_1^{\mathrm{V}}$ and $\mathbf{P}_2^{\mathrm{V}}$.

Out of 40 combinations of hyperparameter configurations, the optimal number of atoms in $\mathbf{D}_1$ and $\mathbf{D}_2$ is determined to be 20, with an optimal sparsity control factor of 0.1. The dictionaries that were trained are presented in Figures 3d,e. Notably, there is a coherence between the texture of atom pairs in the low-resolution dictionary $\mathbf{D}_1$ and the high-resolution dictionary $\mathbf{D}_2$. This coherence is learned from the patches spontaneously rather than predefined. The difference between $\mathbf{P}_2^{\mathrm{T}}$ and the transformed $\hat{\mathbf{P}}_1^{\mathrm{T}}$ is 6.1%, while the difference between $\mathbf{P}_2^{\mathrm{V}}$ and the transformed $\hat{\mathbf{P}}_1^{\mathrm{V}}$ is 7.6%. To evaluate the performance of trained dictionaries, we upsample $\mathcal{M}_1$ to the same resolution as $\mathcal{M}_2$ using bicubic interpolation, and the difference between $\mathcal{M}_2$ and the upsampled $\mathcal{M}_1$ in the overlapping region is 11.55%. The

difference between models decreases on both training and validation sets, indicating the effectiveness of the method. Subsequently, the transformation is applied to the entire region of $\mathcal{M}_1$, and the reconstructed model is shown in Figure 3c. This model is smoother than CVM-S4.26 in the entire domain (Figure 3b) and more consistent with the Z2015 model in the common region. Additionally, the reconstructed model shows a good consistency with geological features, e.g., low velocities around both the San Jacinto and San Andreas faults.

3.3 Transformation between both 3D V_P and V_S models

To demonstrate more general application scenarios, we show the efficacy of our methodology by analyzing 3D velocity models that incorporate both V_P and V_S. Merging and enhancing 3D models can improve derivation of earthquake source properties, simulations of ground motion, and other applications. Additionally, the V_P/V_S ratio is an important parameter that provides key information on various geological and mechanical aspects such as lithology, rock damage, partial melting and water saturation. A seismic velocity model of high quality should display coherent geological features in the V_P/V_S ratios.

Fang et al. (2019) developed a joint inversion technique that utilizes both body and surface wave data to improve the resolution of V_P (Figure 4, middle row) and VS (Figure 5, middle row). The resulting velocity model (referred to as F2019) exhibits distinct regions of V_P/V_S ratios along the coast, in the vicinity of the San Jacinto and San Andreas faults, and the Salton Sea regions (Figure 6, middle row). In contrast, the regional seismic tomography model CVM-S4.26 lacks coherent regions of V_P/V_S ratios consistent with geological features (Figure 6, top row). When transforming an under-constrained V_P/V_S ratio model to a well-constrained model, it is important to verify that the resulting V_P/V_S ratios correlate well with geological features.

In this case study, the initial seismic velocity model $\mathcal{M}_1$ is taken from velocities at 5 different depth sections (1, 2, 3, 4, and 5 km) of the CVM-S4.26, while the target model $\mathcal{M}_2$ is taken from velocities of the F2019 model at the same depths. Both models have two sets of velocities, V_P and V_S, with a total of 10 layers representing values at different depths. The horizontal resolution resolutions of $\mathcal{M}_1$ and $\mathcal{M}_2$ are $0.09^\circ \times 0.09^\circ$ and $0.03^\circ \times 0.03^\circ$, respectively. To ensure the smoothness of the transformed model, we employ bicubic interpolation to upsample $\mathcal{M}_1$ to match the horizontal resolution of $\mathcal{M}_2$. We then extract patches from both models using a $9 \times 9 \times 10$ sliding window (10 being the number of layers) with a stride of 1. The resulting patch pairs total 980, from which 800 are randomly selected for the training set and the remaining pairs are used for validation. Each of our trained dictionaries contain 20 atoms with a dimension of $9 \times 9 \times 10$. After transformation, the difference between $\mathbf{P}_2^{\mathrm{T}}$ and the transformed $\hat{\mathbf{P}}_1^{\mathrm{T}}$ is 2.9%, while the difference between $\mathbf{P}_2^{\mathrm{V}}$ and the transformed $\hat{\mathbf{P}}_1^{\mathrm{V}}$ is 3.4%. As a baseline, the difference between patches extracted from $\mathcal{M}_1$ and $\mathcal{M}_2$ in the overlapping region is 8.1%. Both reconstructions of training and validation patches are more consistent with the target model, compared to the initial model.

The reconstructed V_P/V_S exhibits significant visual improvements with respect to the initial model and enhanced similarity to the target model. The updated regional V_P/V_S results display clearly several zones with coherent values (Figure 6, bottom row), which extend the correlations with geological characteristics shown in the F2019 model. The coherence is also clear in a cross-section that traverses both the San Jacinto and San Andreas faults (Figure 7).

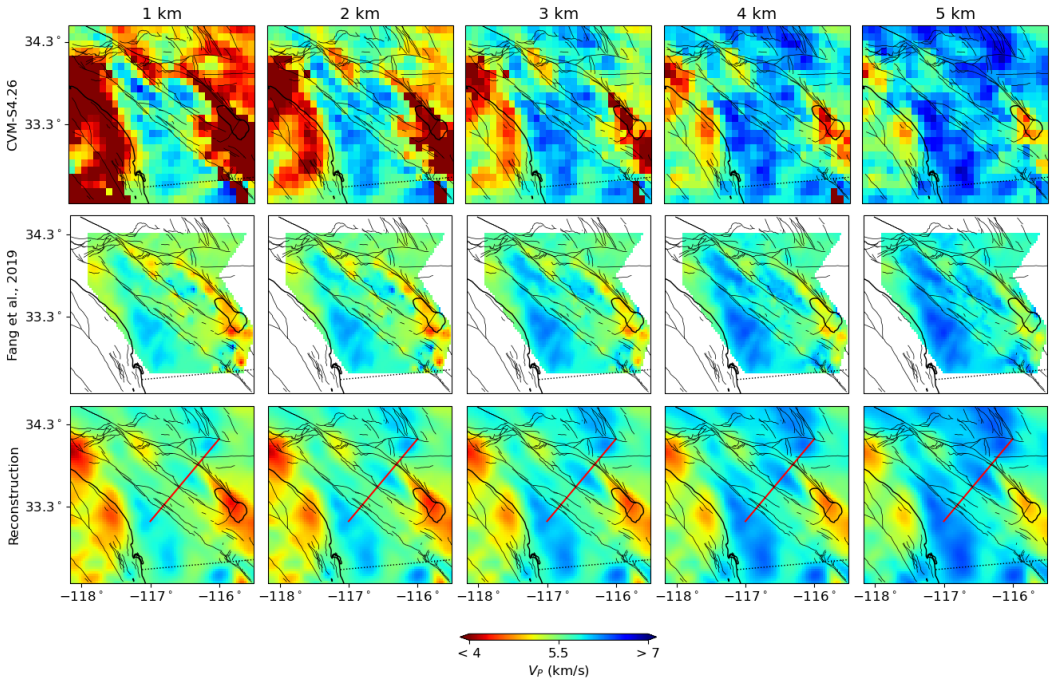

Figure 4. Horizontal slices of V_P at 1, 2, 3, 4, and 5 km depths from CVM-S4.26 (top row), F2019 model (middle row) and the reconstructed model (bottom row). Black lines show major fault traces, as well as the Salton Sea. The red line at the bottom row shows the vertical cross section shown in Figure 7.

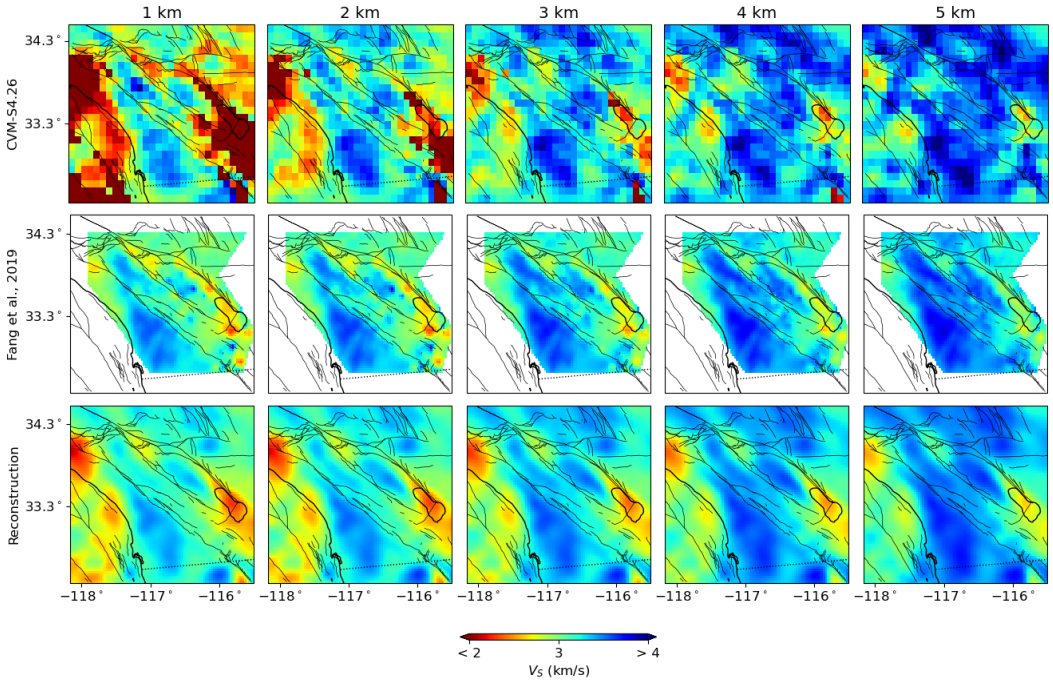

Figure 5. Same as Figure 4 for V_S.

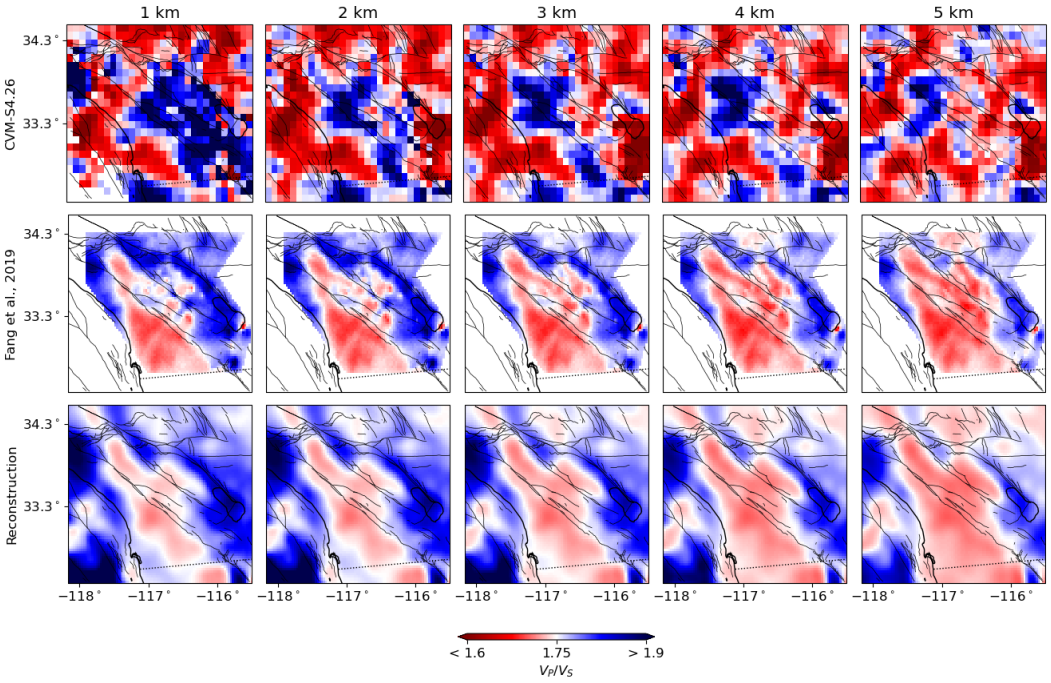

Figure 6. Same as Figure 4 for V_P/V_S.

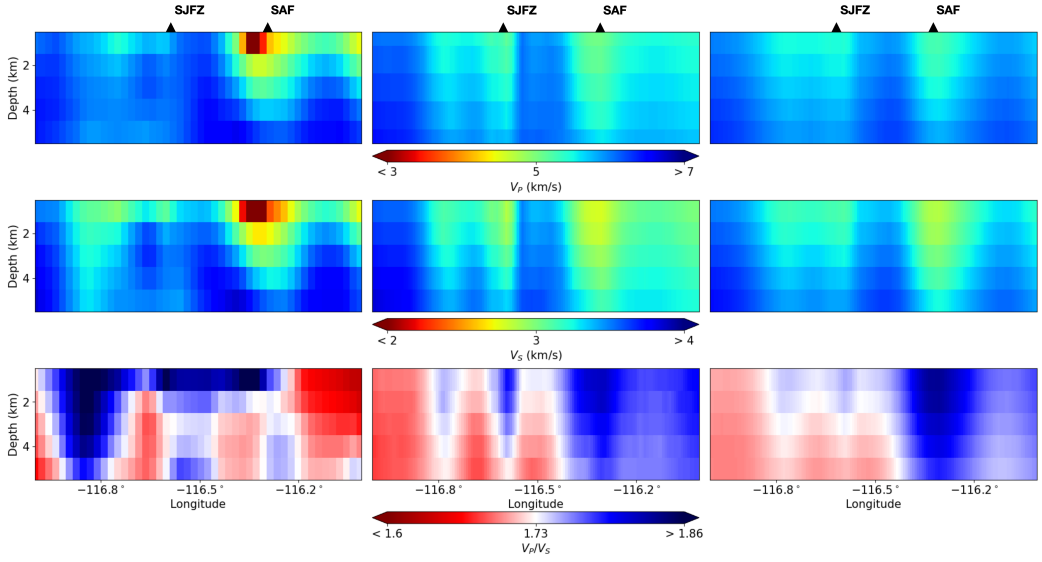

Figure 7. Vertical profiles of V_P (top row), V_S (middle row) and V_P/V_S (bottom row) along the cross-section indicated in Figure 4 in CVM-S4.26 (first column), F2019 model (second column) and the reconstructed model (third column). The locations of the San Andreas Fault (SAF) and San Jacinto Fault Zone (SJFZ) are marked by black triangles.

4 Discussion

We present a method based on sparse dictionary learning for developing transformations between seismic velocity models of different resolutions. The developed technique is used to merge local high-resolution tomographic results within a larger scale lower-resolution model, while simultaneously enhancing the information in the larger scale model. The method is illustrated using V_P, V_S, and V_P/V_S tomographic results of local and regional velocity models in Southern California. The utilized sparse dictionary learning is amenable to interpretation and generalizations. Reconstructed 2D slices and 3D volumes of the regional CVM-S4.26 model (Lee et al., 2014) exhibit visual enhancements and resemblance to results of local higher-resolution target models (Zigone et al., 2015; Fang et al., 2019), which are especially clear for V_P/V_S ratios. The superiority of the reconstructed regional model relative to the original version is demonstrated further below by examining correlations of results with geological features and model validation with numerical simulations of seismic waveforms.

4.1 Interpretability of the dictionary-based method

Sparse dictionary learning is a highly interpretable approach that produces a set of fundamental atoms that can be visualized, and the sparse representation can itself be physically meaningful. For instance, we can define the dominant atom $\boldsymbol{d}_m$ for a given patch $\boldsymbol{p}_j$ as the atom with the largest coefficient in the sparse representation of the patch, i.e., $c_{m,j} = \max(c_{i,j})$, and assign the index of the dominant atom (m) to the center location of the patch. This procedure may be used to classify different regions and obtain a map of dominant atoms distribution which can be further analyzed.

To illustrate, we compare the distribution of the dominant atoms in the results of section 3.3 with velocity profiles and geological features (Figure 8). Patches from areas with low V_P, V_S and high V_P/V_S ratios, such as the north end of SJFZ and around the SAF, mostly have the first atom as the dominant one (red colored in Figure 8)a). To investigate the relationship between atoms and subsurface structures, a cluster analysis is performed on vertical velocity profiles (each profile contains V_P and V_S values over the 1-5 km depth section at a given latitude and longitude) from the F2019 model. The profiles are partitioned into six sets using a K-means algorithm that minimize the inter-cluster variance (Eymold & Jordan, 2019). The spatial distribution of the dominant atoms is correlated with the clusters of seismic velocity profiles; e.g., the green colored area in Figure 8b is consistent with the spatial distribution of first-atom-dominated patches. In addition, the distribution of the dominant atoms is well correlated with the geological map (Figure 8c). The results indicate that the spatial distribution of the first atoms has important information on the geological units and seismic velocities at depth.

Comparing the distribution of the first-atom-dominated patches with the geological map (Figure 8c) shows that it is highly consistent with the distribution of the surface rocks. This consistency further indicates that the surface geological features and rock types are related to the velocity structure at the examined 1-5 km depth sections. The physical interpretability of dictionary learning can thus facilitate establishing correlations between regions in the reconstructed velocity models and geological features.

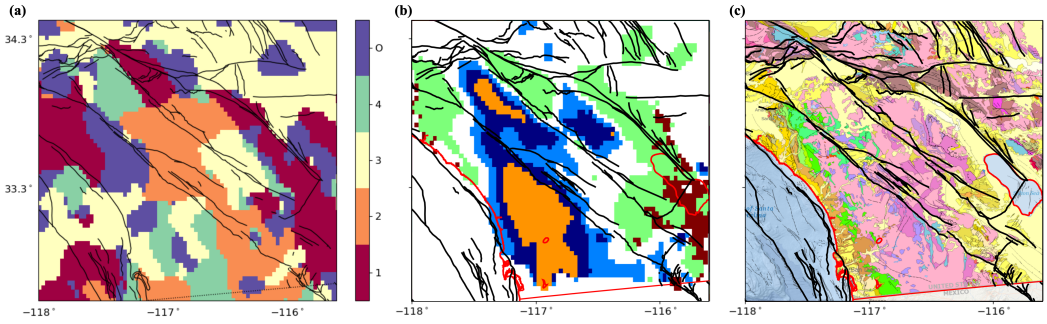

Figure 8. **(a)** Indexes of the dominant atom for the F2019 model in section 3.3. Location of first-atom-dominated patches are colored by dark red. All atoms other than atoms 1-4 are represented by O. **(b)** Clustering of velocity profiles by the K-means algorithm. The cluster corresponding to first-atom-dominated patches is green colored. **(c)** A geological map for Southern California extracted from the website of the California Geological Survey (see Data Availability). The main rock types in the study region are: Continental sedimentary rocks (light yellow), plutonic rocks (pink) and metavolcanic rocks (green).

4.2 Validation of the reconstructed model

To demonstrate further the utility of the presented method, we compare waveform simulation results using the reconstructed model and CVM-S4.26 for a test earthquake (Figure 9a). The hypocentre location of this M4.4 event (Event ID: 38245496) is taken from the relocated catalog of Hauksson et al. (2012, extended to later years) and the moment tensor solution used in the simulation is taken from the catalog of Wang and Zhan (2020). The reconstructed model used in this simulation is obtained by transforming the top 10 km of CVM-S4.26 to the F2019 model using the same dictionary learning approach described in section 3.3. To have a more representative comparison, we also interpolate the top 10 km of CVM-S4.26 to the same resolution as F2019 and refer to this as a baseline model. Since the first layer of both the reconstructed and baseline models are at 1 km depth, we extract the surface velocities from CVM-S4.26 and add them on top of both models. As in Lu and Ben-Zion (2022), the surface topography is implemented by deforming the mesh grid in the vertical direction. Since the F2019 model only provides seismic velocities, we approximate the density (ρ) and quality factors (Q_P, Q_S) using empirical results from (Brocher, 2005) and (Taborda et al., 2016).

The simulations use the SPECFEM3D code (Komatitsch & Tromp, 2002) to compute synthetic waveforms at 3 stations (CI.HEC, CI.BBR, and CI.IKP). The simulation domain is centered at coordinates $(116.53°W, 33.64°N)$ and has a lateral dimension of 320 km $\times$ 280 km in the local Cartesian coordinate (Li et al., 2022). The number of spectral elements along both x and y is 256, making the simulation domain as dense as the grid of the CVM-S4.26 and reconstructed models. We compare observed waveforms and synthetic waveforms in the period band of 0.4-2 Hz, which allows us to focus on the depth range of the enhanced velocity model. As demonstrated in Figure 9, the simulation results based on the reconstructed model exhibit a closer fit to the observations than those produced using the baseline model for both the body waves and surface waves portions of the seismograms. This improvement

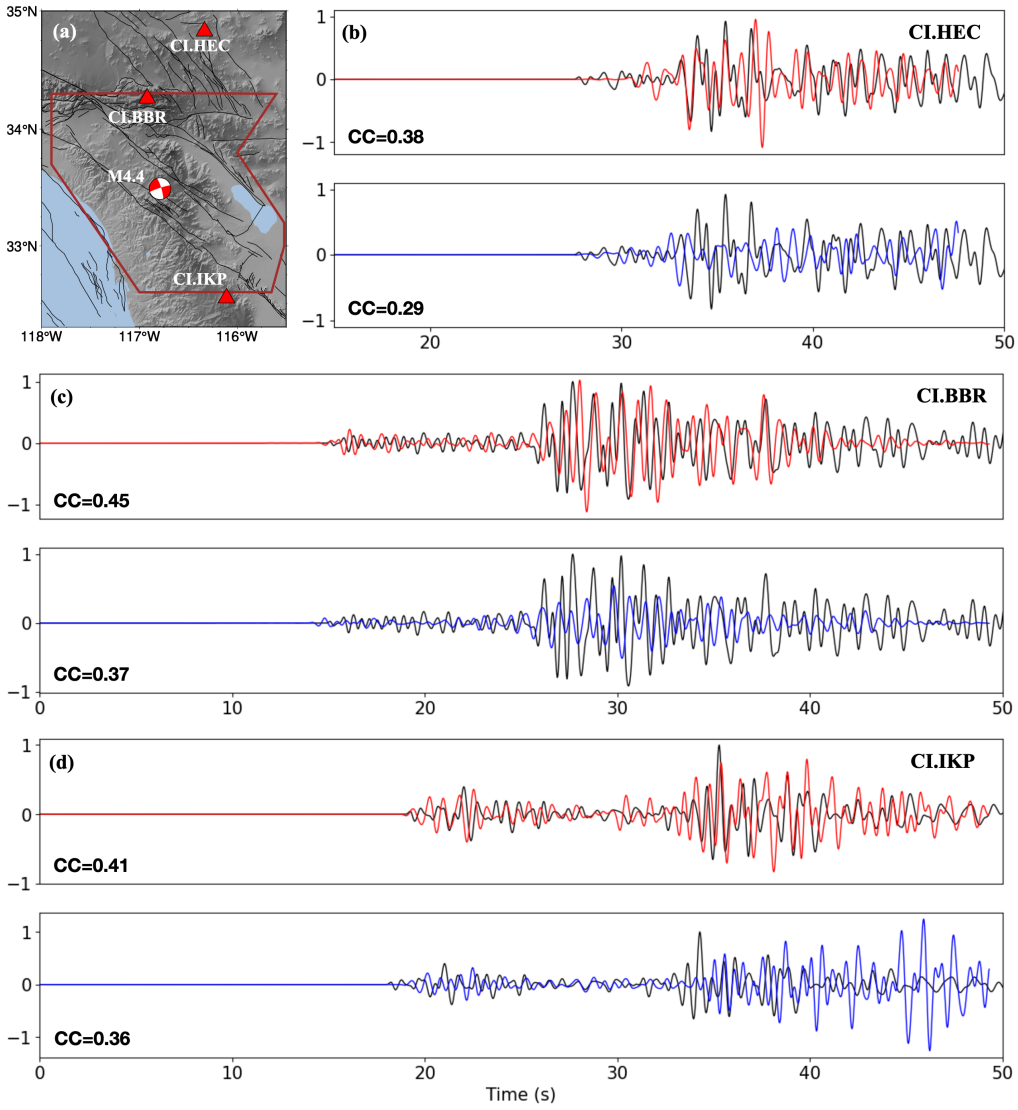

Figure 9. **(a)** Locations of the event and stations (CI.HEC, CI.BBR, and CI.IKP) used for validation. Black lines show major fault traces. The red polygon represents the coverage of the F2019 model. **(b-d)** Vertical components of observational (black lines) and synthetic waveforms at station CI.HEC (b), CI.BBR (c), and CI.IKP (d). The synthetic waveforms are computed for both the reconstructed model (red lines) and the baseline model (CVM-S4.26, blue lines). The CC between observations and simulations are denoted on the bottom-left corner of each panel. All waveforms are bandpass filtered from 0.4 to 2 Hz normalized and by the maximum amplitude of the observed waveform.

is also supported by an increase in the CC between the synthetic and observed waveforms and it exists also for stations outside the common region. The close fit of the simulated amplitude of multiple phases to data indicates that the reconstructed model can improve predictions of earthquake ground motion.

4.3 Limitatioins and outlook for future research

The developed sparse dictionary learning method for transferring high-resolution seismic velocity results to lower velocity models is shown to be effective, but it has several limitations. First, the method requires a local seismic velocity model of high quality, which may not always be available. Furthermore, factors such as overall consistency between the regional and local models, as well as the resolution, coverage, and geological features in the data utilized, can influence the quality of the trained dictionaries and the reconstructed models. Additionally, the selection of hyper-parameters (section 2.2) may vary for different models and should be tuned through experimentation and validation. In the present work we aimed primarily to develop and illustrate the method, and have conducted only example waveform simulations for validation. A future study will include a more comprehensive validation using multiple earthquakes, virtual seismic noise sources, and many stations.

The developed method for merging and enhancing velocity models can be applied to other regions that have well-developed regional seismic velocity models and local high quality models, such as northern California, Europe and Japan. The improved multi-scale velocity models can have numerous applications in the field of seismology. Examples include more accurate derivation of earthquake source properties and more realistic simulations of ground motion over a wider range of frequencies leading to better estimates of seismic hazard. The concept of dictionary representation and transformation presented in this paper can be applied to additional earth science datasets. For instance, high-resolution surface deformation observed from InSAR is limited to areas with high correlations not including, for example, highly vegetated regions (e.g. Wei & Sandwell, 2010). An approach similar to the one developed in this paper can enhance regional low-resolution deformation observations with higher-resolution local results. Furthermore, the low temporal resolution of InSAR data can be improved by high temporal resolution GPS data regarding the timeline as an extra dimension (e.g. Xu et al., 2022). The interpretability of the dictionary learning method can also allow discovering spatial and temporal correlations between different physical quantities, such as geological features, seismic velocity structure and surface deformation.

Data Availability

The CVM-S4.26 model is available on the UCVM software provided by the Southern California Earthquake Center (`https://www.scec.org/software/ucvm`). Other seismic velocity models used in this study are from Zigone et al. (2015) and Fang et al. (2019). The earthquake waveform data used in this paper is retrieved from the data center of the southern California network CI (`https://scedc.caltech.edu/data`). The geological data in Figure 8 were obtained from the CGS website (`https://maps.conservation.ca.gov/cgs/gmc/`).

Acknowledgments

We thank Guoliang Li for help with the waveform simulations. This research is supported by the U.S. Department of Energy (Award DE-SC0016520).

References

Ajala, R., & Persaud, P. (2021). Effect of Merging Multiscale Models on Seismic Wavefield Predictions Near the Southern San Andreas Fault. *Journal of Geophysical Research: Solid Earth*, *126*(10), e2021JB021915. doi: doi:10.1029/2021JB021915

Allam, A. A., & Ben-Zion, Y. (2012). Seismic velocity structures in the southern California plate-boundary environment from double-difference tomography. *Geophysical Journal International*, *190*(2), 1181-1196. doi: doi:10.1111/j.1365-246X.2012.05544.x

Beckouche, S., & Ma, J. (2014). Simultaneous dictionary learning and denoising for seismic data. *GEOPHYSICS*, *79*(3), A27-A31. doi: doi:10.1190/geo2013-0382.1

Bianco, M. J., & Gerstoft, P. (2018). Travel time tomography with adaptive dictionaries. *IEEE Transactions on Computational Imaging*, *4*(4), 499-511. doi: doi:10.1109/TCI.2018.2862644

Bonilla, L. F., Steidl, J. H., Gariel, J.-C., & Archuleta, R. J. (2002). Borehole Response Studies at the Garner Valley Downhole Array, Southern California. *Bulletin of the Seismological Society of America*, *92*(8), 3165-3179. doi: doi:10.1785/0120010235

Brocher, T. M. (2005). Empirical Relations between Elastic Wavespeeds and Density in the Earth's Crust. *Bulletin of the Seismological Society of America*, *95*(6), 2081–2092. doi: doi:10.1785/0120050077

Dong, C., Loy, C. C., He, K., & Tang, X. (2015). *Image super-resolution using deep convolutional networks.* arXiv. doi: doi:10.48550/ARXIV.1501.00092

Eymold, W. K., & Jordan, T. H. (2019). Tectonic Regionalization of the Southern California Crust From Tomographic Cluster Analysis. *Journal of Geophysical Research: Solid Earth*, *124*(11), 11840–11865. doi: doi:10.1029/2019JB018423

Fang, H., White, M. C. A., Lu, Y., & Ben-Zion, Y. (2022). Seismic traveltime tomography of southern california using poisson-voronoi cells and 20 years of data. *Journal of Geophysical Research: Solid Earth*, *127*(5), e2021JB023307. doi: doi:10.1029/2021JB023307

Fang, H., Yao, H., Zhang, H., Thurber, C., Ben-Zion, Y., & van der Hilst, R. D. (2019). Vp/Vs tomography in the southern California plate boundary region using body and surface wave traveltime data. *Geophysical Journal International*, *216*(1), 609–620. doi: doi:10.1093/gji/ggy458

Fichtner, A., van Herwaarden, D.-P., Afanasiev, M., Simutė, S., Krischer, L., Çubuk Sabuncu, Y., ... Igel, H. (2018). The Collaborative Seismic Earth Model: Generation 1. *Geophysical Research Letters*, *45*(9), 4007–4016. doi: doi:10.1029/2018GL077338

Gatys, L. A., Ecker, A. S., & Bethge, M. (2016, June). Image style transfer using convolutional neural networks. In *Proceedings of the ieee conference on computer vision and pattern recognition (cvpr).*

Gibbs, J. F., Boore, D. M., Tinsley III, J. C., & Mueller, C. S. (2001). *Borehole P- and S-wave velocity at thirteen stations in Southern California* (Report No. 2001-506). Reston, VA. doi: doi:10.3133/ofr01506

Hauksson, E., Yang, W., & Shearer, P. M. (2012). Waveform Relocated Earthquake Catalog for Southern California (1981 to June 2011). *Bulletin of the Seismological Society of America*, *102*(5), 2239–2244. doi: doi:10.1785/0120120010

Hillers, G., Roux, P., Campillo, M., & Ben-Zion, Y. (2016). Focal spot imaging based on zero lag cross-correlation amplitude fields: Application to dense array data at the san jacinto fault zone. *Journal of Geophysical Research: Solid Earth*, *121*(11). doi: doi:10.1002/2016JB013014

Juarez, A., & Ben-Zion, Y. (2020). Effects of Shallow-Velocity Reductions on 3D Prop-

agation of Seismic Waves. *Seismological Research Letters*, *91*(6), 3313–3322. doi: doi:10.1785/0220200183

Komatitsch, D., & Tromp, J. (2002). Spectral-element simulations of global seismic wave propagation—I. Validation. *Geophysical Journal International*, *149*(2), 390–412. doi: doi:10.1046/j.1365-246X.2002.01653.x

Kreutz-Delgado, K., Murray, J. F., Rao, B. D., Engan, K., Lee, T.-W., & Sejnowski, T. J. (2003). Dictionary Learning Algorithms for Sparse Representation. *Neural Computation*, *15*(2), 349–396. doi: doi:10.1162/089976603762552951

Lee, E.-J., Chen, P., Jordan, T. H., Maechling, P. B., Denolle, M. A. M., & Beroza, G. C. (2014). Full-3-d tomography for crustal structure in southern california based on the scattering-integral and the adjoint-wavefield methods. *Journal of Geophysical Research: Solid Earth*, *119*(8), 6421-6451. doi: doi:10.1002/2014JB011346

Li, G., Tao, K., Chen, M., Li, J., Maguire, R., & Ma, X. (2022). Cartesian Meshing Spherical Earth (CMSE): A Code Package to Incorporate the Spherical Earth in SPECFEM3D Cartesian Simulations. *Seismological Research Letters*, *93*(2A), 986-996. doi: doi:10.1785/0220210131

Lu, Y., & Ben-Zion, Y. (2022). Validation of seismic velocity models in southern California with full-waveform simulations. *Geophysical Journal International*, *229*(2), 1232–1254. doi: doi:10.1093/gji/ggab534

Mairal, J., Bach, F., Ponce, J., & Sapiro, G. (2009). Online dictionary learning for sparse coding. In *Proceedings of the 26th annual international conference on machine learning* (pp. 689–696).

Mallat, S., & Zhang, Z. (1993). Matching pursuits with time-frequency dictionaries. *IEEE Transactions on Signal Processing*, *41*(12). doi: doi:10.1109/78.258082

Mordret, A., Roux, P., Boué, P., & Ben-Zion, Y. (2019). Shallow three-dimensional structure of the San Jacinto fault zone revealed from ambient noise imaging with a dense seismic array. *Geophysical Journal International*, *216*(2), 896-905. doi: doi:10.1093/gji/ggy464

Rubinstein, R., Bruckstein, A. M., & Elad, M. (2010). Dictionaries for Sparse Representation Modeling. *Proceedings of the IEEE*, *98*(6), 1045–1057. doi: doi:10.1109/JPROC.2010.2040551

Share, P.-E., Allam, A. A., Ben-Zion, Y., Lin, F.-C., & Vernon, F. L. (2019). Structural Properties of the San Jacinto Fault Zone at Blackburn Saddle from Seismic Data of a Dense Linear Array. *Pure and Applied Geophysics*, *176*(3), 1169–1191. doi: doi:10.1007/s00024-018-1988-5

Shaw, J. H., Plesch, A., Tape, C., Suess, M. P., Jordan, T. H., Ely, G., ... Munster, J. (2015). Unified structural representation of the southern california crust and upper mantle. *Earth and Planetary Science Letters*, *415*, 1-15. doi: doi:10.1016/j.epsl.2015.01.016

Sulam, J., You, C., & Zhu, Z. (2020). *Recovery and Generalization in Over-Realized Dictionary Learning.* Retrieved from http://arxiv.org/abs/2006.06179 doi: doi:10.48550/arXiv.2006.06179

Taborda, R., Azizzadeh-Roodpish, S., Khoshnevis, N., & Cheng, K. (2016). Evaluation of the southern California seismic velocity models through simulation of recorded events. *Geophysical Journal International*, *205*(3), 1342–1364. doi: doi:10.1093/gji/ggw085

Tibshirani, R. (1996). Regression Shrinkage and Selection via the Lasso. *Journal of the Royal Statistical Society. Series B (Methodological)*, *58*(1), 267–288.

Wang, X., & Zhan, Z. (2020). Moving from 1-D to 3-D velocity model: automated waveform-

based earthquake moment tensor inversion in the Los Angeles region. *Geophysical Journal International*, *220*(1), 218-234. doi: doi:10.1093/gji/ggz435

Wei, M., & Sandwell, D. T. (2010). Decorrelation of l-band and c-band interferometry over vegetated areas in california. *IEEE Transactions on Geoscience and Remote Sensing*, *48*(7), 2942-2952. doi: doi:10.1109/TGRS.2010.2043442

Xu, X., Hua, R., & Guns, K. A. (2022). Predicting InSAR deformation with GNSS using machine learning. In *AGU fall meeting abstracts* (Vol. 2022, p. G45A-01).

Yang, J., Wright, J., Huang, T., & Ma, Y. (2008). Image super-resolution as sparse representation of raw image patches. In *2008 ieee conference on computer vision and pattern recognition* (p. 1-8). doi: doi:10.1109/CVPR.2008.4587647

Yeh, T.-Y., & Olsen, K. B. (2022). Data-constrained fault zone structure improves 0-3 Hz deterministic ground motion predictions for the 2019 M7.1 Ridgecrest earthquake. In *Poster Presentation at 2022 SCEC Annual Meeting.*

Zigone, D., Ben-Zion, Y., Campillo, M., & Roux, P. (2015). Seismic Tomography of the Southern California Plate Boundary Region from Noise-Based Rayleigh and Love Waves. *Pure and Applied Geophysics*, *172*(5), 1007–1032. doi: doi:10.1007/s00024-014-0872-1